Modeling soil evaporation efficiency in a range of soil and atmospheric conditions using a meta-analysis approach

Olivier Merlin, Vivien Stefan, A Amazirh, A Chanzy, Eric Ceschia, S Er-Raki, P Gentine, Tiphaine Tallec, J Ezzahar, Simone Bircher, et al.

AGU PUBLICATIONS

Water Resources Research

RESEARCH ARTICLE

10.1002/2015WR018233

Key Points:

- The new soil resistance model is based on soil moisture and two observable parameters
- Models are tested using a data set composed of more than 30 contrasted sites
- One resistance parameter is significantly correlated with both sand and clay fractions

Correspondence to:
O. Merlin,
olivier.merlin@cesbio.cnes.fr

Citation:
Merlin, O., et al. (2016), Modeling soil evaporation efficiency in a range of soil and atmospheric conditions using a meta-analysis approach, *Water Resour. Res.*, *52*, doi:10.1002/2015WR018233.

Received 13 OCT 2015
Accepted 12 APR 2016
Accepted article online 20 APR 2016

Modeling soil evaporation efficiency in a range of soil and atmospheric conditions using a meta-analysis approach

O. Merlin[1,2], V. G. Stefan[1], A. Amazirh[2], A. Chanzy[3], E. Ceschia[1], S. Er-Raki[2], P. Gentine[4], T. Tallec[1], J. Ezzahar[2], S. Bircher[1], J. Beringer[5], and S. Khabba[2]

[1]CESBIO, Université de Toulouse, CNES, CNRS, IRD, UPS, Toulouse, France, [2]Faculté des Sciences et Techniques, University of Cadi Ayyad, Marrakech, Morocco, [3]EMMAH, INRA, Université d'Avignon et des Pays de Vaucluse, 84000, Avignon, France, [4]Department of Earth and Environmental Engineering, Columbia University, New York City, New York, USA, [5]School of Earth and Environment, University of Western Australia, Perth, Australia

Abstract A meta-analysis data-driven approach is developed to represent the soil evaporative efficiency (SEE) defined as the ratio of actual to potential soil evaporation. The new model is tested across a bare soil database composed of more than 30 sites around the world, a clay fraction range of 0.02–0.56, a sand fraction range of 0.05–0.92, and about 30,000 acquisition times. SEE is modeled using a soil resistance (r_{ss}) formulation based on surface soil moisture (θ) and two resistance parameters $r_{ss,ref}$ and $\theta_{efolding}$. The data-driven approach aims to express both parameters as a function of observable data including meteorological forcing, cut-off soil moisture value $\theta_{1/2}$ at which SEE=0.5, and first derivative of SEE at $\theta_{1/2}$, named $\Delta\theta_{1/2}^{-1}$. An analytical relationship between $(r_{ss,ref};\theta_{efolding})$ and $(\theta_{1/2};\Delta\theta_{1/2}^{-1})$ is first built by running a soil energy balance model for two extreme conditions with $r_{ss}=0$ and $r_{ss}\sim\infty$ using meteorological forcing solely, and by approaching the middle point from the two (wet and dry) reference points. Two different methods are then investigated to estimate the pair $(\theta_{1/2};\Delta\theta_{1/2}^{-1})$ either from the time series of SEE and θ observations for a given site, or using the soil texture information for all sites. The first method is based on an algorithm specifically designed to accomodate for strongly nonlinear SEE(θ) relationships and potentially large random deviations of observed SEE from the mean observed SEE(θ). The second method parameterizes $\theta_{1/2}$ as a multi-linear regression of clay and sand percentages, and sets $\Delta\theta_{1/2}^{-1}$ to a constant mean value for all sites. The new model significantly outperformed the evaporation modules of ISBA (Interaction Sol-Biosphère-Atmosphère), H-TESSEL (Hydrology-Tiled ECMWF Scheme for Surface Exchange over Land), and CLM (Community Land Model). It has potential for integration in various land-surface schemes, and real calibration capabilities using combined thermal and microwave remote sensing data.

1. Introduction

Evaporation accounts for approximately 20–40% of the global evapotranspiration [*Lawrence et al.*, 2007; *Schlesinger and Jasechko*, 2014] and originates mainly (65%) from soils rather than surface waters [*Good et al.*, 2015]. As an important boundary condition between the soil and atmosphere, soil evaporation is explicitly represented in a range of agronomic, hydrological, meteorological and climate models at multiple scales: from the crop field [e.g., *Allen*, 2000], to the catchment [e.g., *Wood et al.*, 1992] and to the mesoscale [e.g., *Sakaguchi and Zeng*, 2009]. Accurate estimations of soil evaporation are notably needed to quantify the partitioning of evapotranspiration into soil evaporation and plant evaporation and transpiration [*Williams et al.*, 2004; *Kool et al.*, 2014]. Such partitioning is fundamental to monitor vegetation water uptake and stress [*Porporato et al.*, 2001; *Er-Raki et al.*, 2010] within an environment of scarse water resources, and to better understand land-atmosphere interactions [*Feddes et al.*, 2001; *Er-Raki et al.*, 2010]. This is especially true in sparsely vegetated areas such as arid and semi-arid regions, and agricultural fields during bare or partially covered soil periods.

The evaporation of unsaturated soils is a complex process due to the coupling of the energy and mass transfers at the soil-atmosphere interface, which involves liquid and vapor transport in the near-surface soil pores, incident solar energy for phase change, and vapor transfer across the boundary layer [*Philip and de Vries*, 1957; *Milly*, 1984; *Chanzy and Bruckler*, 1993; *Bittelli et al.*, 2008; *Smits et al.*, 2012; *Or et al.*, 2013]. The soil control on evaporation originates from two main processes: the difference in water vapor concentrations (Cw) between the evaporative surface and atmosphere, and the soil vapor diffusion when the evaporative sources are located below the soil surface. The vapor diffusion depends on the depth, degree of saturation and temperature of the evaporative site. Comprehensive physical models as those based on Philip and de Vries equations can represent both temperature and water potential gradients as well as vapor diffusion. Such models are driven by standard climatic conditions but are, however, very sensitive to soil hydraulic properties (SHPs), initialization and bottom boundary conditions [*Chanzy et al*., 2008]. These characteristics hamper the implementation of comprehensive models to represent large areas, as it requires numerous simulation units and the capability of characterizing soil parameters in every unit. The most common alternative is to use evaporation models related to the surface soil moisture. Considering the physical processes mentioned above, soil moisture is only a proxy of the soil quantities that control the evaporation rate. For instance, we have to consider all evaporation sites -which may be located at different levels in the soil- as well as the water potential/water content relationships. These properties are linked to the soil surface wetness but can also be governed by other factors such as the climatic demand or the soil surface structure. Moreover the thickness of the layer considered to characterize moisture has also an impact on the evaporation models' parameters.

There are numerous evaporation models that are based on soil moisture. They all try to represent the limitation of evaporation by soil moisture (water) and evaporative demand, generally using empirical or semi-empirical approaches [*Viterbo and Beljaars*, 1995; *Pitman*, 2003]. Historically, the evaporation module of the so-called Bucket model [*Manabe*, 1969; *Robock et al*., 1995] has been:

$$\mathrm{SEE}=\theta/\theta_c \tag{1}$$

with SEE being the soil evaporative efficiency defined as the actual to potential soil evaporation ratio, θ (m^3 m^{-3}) the surface soil moisture, and θ_c (m^3 m^{-3}) a parameter equal to 0.75 times the soil moisture at field capacity. Since the development of the Bucket model, various attempts have been made to improve the above representation, notably by separating soil and vegetation components using dual-source formulations [*Shuttleworth and Wallace*, 1985]. Soil evaporation is now typically modeled using one of the four following methods, namely the soil surface resistance (r_{ss}) formulation:

$$LE(r_{ss})=\frac{\rho C_P}{\gamma}\times\frac{e_{sat}(T)-e_a}{r_{ah}+r_{ss}} \tag{2}$$

the α formulation:

$$LE(\alpha)=\frac{\rho C_P}{\gamma}\times\frac{\alpha e_{sat}(T)-e_a}{r_{ah}} \tag{3}$$

the β formulation:

$$LE(\beta)=\beta\times\frac{\rho C_P}{\gamma}\times\frac{e_{sat}(T)-e_a}{r_{ah}} \tag{4}$$

or the threshold (LE_{max}) formulation:

$$LE(LE_{max})=\min\left(LEp, LE_{max}\right) \tag{5}$$

with LE (W m^{-2}) being the soil latent heat flux, r_{ss} (s m^{-1}) the resistance to the diffusion of vapor in large soil pores, α a factor (typically ranging from 0 to 1) that scales the saturated vapor pressure down to the actual vapor pressure at the soil surface, β a factor (typically ranging from 0 to 1) that scales potential evaporation down to actual evaporation, ρ (kg m^{-3}) the density of air, C_P (J kg^{-1} K^{-1}) the specific heat capacity of air, γ (Pa K^{-1}) the psychrometric constant, $e_{sat}(T)$ (Pa) the saturated vapor pressure at the soil surface, T (K) the soil surface temperature, e_a (Pa) the vapor pressure of air, r_{ah} (s m^{-1}) the aerodynamic resistance to heat transfer, LEp (W m^{-2}) the potential soil evaporation, and LE_{max} (W m^{-2}) the maximum soil-limited water flux from below the surface. Depending on the authors, the threshold method is also called demand-supply or Priestley-Taylor method and LEp is estimated using the aerodynamic, Penman, or Priestley-Taylor methods. The LE_{max} formulation is equivalent to the β formulation if LE_{max} is parameterized as a fraction of LEp. Note that LE can also be modeled by combining both r_{ss} and α formulations:

$$LE(r_{ss},\alpha)=\frac{\rho C_P}{\gamma}\times\frac{\alpha e_{sat}(T)-e_a}{r_{ah}+r_{ss}}, \tag{6}$$

or both β and α formulations:

$$LE(\beta,\alpha)=\beta\times\frac{\rho C_P}{\gamma}\times\frac{\alpha e_{sat}(T)-e_a}{r_{ah}}. \quad (7)$$

Comprehensive overview of the α, β, r_{ss}, and LE_{max} methods can be found in *Mahfouf and Noilhan* [1991], *Lee and Pielke* [1992], *Ye and Pielke* [1993], *Mihailovic et al.* [1995], *Dekic et al.* [1995] and *Cahill et al.* [1999]. The form of α, β, r_{ss} or LE_{max} is obtained either physically or empirically. Physically based expressions are derived from thermodynamical considerations [*Philip and de Vries*, 1957] or by simplifying the Fick's law of diffusion [e.g., *Dickinson et al.*, 1986; *Wetzel and Chang*, 1988; *Sakaguchi and Zeng*, 2009]. All of them simplify the physics underlying the evaporation process and require some empirism to overcome the assumptions. For instance, simplifications of the theoretical diffusion equation require some empirical parameters in addition to SHPs [*Sakaguchi and Zeng*, 2009]. Empirical models are based on ad hoc expressions [e.g., *Manabe*, 1969; *Noilhan and Planton*, 1989] or curve fitting using limited experimental data [e.g., *Sun*, 1982; *Sellers et al.*, 1992]. Although many different formulations have been developed since the 60's, there is still no consensus on the best way to parameterize evaporation over large areas [*Desborough et al.*, 1996; *Sakaguchi and Zeng*, 2009]. Nevertheless the literature has indicated that (1) existing θ-based formulations differ in four main aspects: the θ lower and upper threshold values, the nonlinearity of the relationship between evaporation and θ, the required input data other than θ, and the sensing depth of θ data, (2) simple empirical expressions may provide better evaporation simulations than physically derived formulations [*Dekic et al.*, 1995; *Mihailovic et al.*, 1995; *Yang et al.*, 1998], (3) the β formulation seems to be more robust than the α one [*Cahill et al.*, 1999; *Van den Hurk et al.*, 2000], and (4) very little work has been done to evaluate the above formulations with observations over a range of soil and atmospheric conditions.

Phenomenological models are distinct from the above simplified models because they are not derived from theory and they are not built on ad hoc assumptions. Phenomenological models are based on observational data rather than theoretical considerations [*Sivapalan et al.*, 2003], but they provide a physical or semi-physical interpretation of model parameters. *Komatsu* [2003] made a first attempt to relate an experimental parameter to soil texture and aerodynamic conditions. However, their study was based on a surface layer of several millimeters, which is much thinner than the top soil thickness (typically several cm) represented by most land-surface models. Moreover, one major difficulty in parameterizing SEE with sufficient generality is the drying (usually around noon) of the top few millimeters of soil which inhibits evaporation, regardless of the availability of soil water underneath [*Mahrt and Pan*, 1984; *Dickinson et al.*, 1986; *Soarès et al.*, 1988; *Wetzel and Chang*, 1988; *Van de Griend and Owe*, 1994; *Heitman et al.*, 2008; *Shahraeeni et al.*, 2012]. This was the rationale for developing a new SEE formulation with a shape that adapts to the depth of θ measurements. The study in *Merlin et al.* [2011] provides an insight into ways of taking into account the soil moisture gradient in the topsoil using a simple parameterization as a function of potential evaporation. Their SEE model was evaluated at the daily time scale at two sites located in the same area (southwestern France).

In the vein of *Komatsu* [2003] and *Merlin et al.* [2011], this paper aims to develop a formulation of quasi-instantaneous SEE that builds upon a multi-site data set including a range of soil and atmospheric conditions. This study notably takes advantage of local, regional and global monitoring networks (e.g., AmeriFlux, European Flux Database), which allow to improve models. A new evaporation model is evaluated in terms of SEE estimates over the wide soil texture range observed within the multi-site data set, and is compared with the evaporation modules of three reference land-surface schemes: ISBA (Interaction Sol-Biosphère-Atmosphère) [*Noilhan and Planton*, 1989], CLM (Community Land Model) [*Oleson et al.*, 2013], and H-TESSEL (Hydrology-Tiled ECMWF Scheme for Surface Exchange over Land) [*ECMWF*, 2014]. Note that all evaporation modules are implemented in the same energy budget model, using the same forcing data, to ensure that the four models are run in identical conditions.

2. Sites and Data Description

The data set comprises 34 sites distributed in 13 countries (see Table 1). Those sites were or have been developed in the frame of national and international flux station networks (AmeriFlux, FluxNet, European Flux Database, OzNet), long term observatories such as AMMA (African Monsoon Multidisciplinary Analysis), HOBE (Danish Hydrological Observatory) and SudMed (South Mediterranean Observatory), or short term

Table 1. Flux Sites Including One or Several "Bare Soil" Periods

Site	Exp./Net.	Lat;lon	Land cover	θ (cm)	f_{clay}	f_{sand}	Reference
AUStu	OzFlux	−17.15;133.35	grass	5	0.145	0.343	*Beringer et al.* [2011]
BELon	GHGEurope	50.55;4.74	crop	5	0.20	0.075	*Papale et al.* [2006]
CHOe2	GHGEurope	47.29;7.73	crop	5	0.43	0.095	*Alaoui and Goetz* [2008]
DEGeb	GHGEurope	51.10;10.91	crop	5	0.30	0.095	*Kutsch et al.* [2010]
DEKli	GHGEurope	50.89;13.52	crop	5	0.557	0.215	*Kindler et al.* [2011]
DESeh	GHGEurope	50.87;6.45	crop	5	0.122	0.168	*Papale et al.* [2006]
DKVou	HOBE	56.04;9.16	crop	2.5	0.02	0.92	*Bircher et al.* [2012]
ESEFE	EFEDA	39.07; −2.11	bare	10	0.20	0.19	*Braud et al.* [1993]
ESES2	GHGEurope	39.28; −0.32	crop	5	0.475	0.104	*Kutsch et al.* [2010]
FRAur	GHGEurope	43.55;1.11	crop	5	0.323	0.206	*Béziat et al.* [2009]
FRAvi	GHGEurope	43.92;4.88	crop	5	0.328	0.132	*Garrigues et al.* [2015]
FRGri	GHGEurope	48.84;1.95	crop	5	0.189	0.098	*Van den Hoof et al.* [2011]
FRLam	GHGEurope	43.50;1.24	crop	5	0.543	0.12	*Béziat et al.* [2009]
FRRe1	ReSeDa	43.79;4.74	crop	2.5	0.40	0.05	*Olioso et al.* [2002]
FRRe2	ReSeDa	43.79;4.74	crop	2.5	0.40	0.05	*Olioso et al.* [2002]
IECa1	GHGEurope	52.86; −6.92	crop	5	0.17	0.57	*Walmsley et al.* [2011]
ITBCi	GHGEurope	40.52;14.96	crop	5	0.46	0.32	*Denef et al.* [2013]
ITCas	GHGEurope	45.20;9.67	crop	5	0.22	0.25	*Denef et al.* [2013]
ITRo4	GHGEurope	42.37;11.92	crop	5	0.382	0.301	*Marchesini et al.* [2008]
MEYaq	Yaqui'08	27.27; −109.88	crop	5	0.44	0.36	*Chirouze et al.* [2014]
MOSR1	SudMed	31.67; −7.59	crop	5	0.47	0.185	*Er-Raki et al.* [2007]
MOSR2	SudMed	31.67; −7.61	crop	5	0.47	0.185	*Jarlan et al.* [2015]
NIDeg	AMMA	13.65;2.64	bare	10	0.08	0.77	*Pellarin et al.* [2009]
NIHAP	HAPEX	2.24;13.20	bare	5	0.057	0.93	*Wallace et al.* [1993]
NIMil	AMMA	13.64;2.63	crop	10	0.08	0.77	*Pellarin et al.* [2009]
NISav	AMMA	13.65;2.63	fallow	10	0.08	0.77	*Pellarin et al.* [2009]
USArm	AmeriFlux	36.61; −97.49	crop	5	0.43	0.28	*Fischer et al.* [2007]
USDk1	AmeriFlux	35.97; −79.09	grass	10	0.09	0.48	*Novick et al.* [2004]
USFwf	AmeriFlux	35.45; −111.77	grass	2	0.13	0.30	*Dore et al.* [2012]
USIb1	AmeriFlux	41.86; −88.22	crop	2.5	0.35	0.10	*Wu et al.* [2012]
USIHO	IHOP	36.47; 100.62	bare	5	0.28	0.58	*Lemone et al.* [2007]
USMo1	Monsoon'90	31.74; −110.05	shrub	5	0.10	0.66	*Santanello et al.* [2007]
USMo7	Monsoon'90	31.72; −110.01	shrub	5	0.06	0.80	*Santanello et al.* [2007]
USSGP	SGP'97	35.54; −98.06	bare	5	0.24	0.26	*Timmermans et al.* [2007]

intensive field campaigns such as EFEDA (Echival Field Experiment in a Desertification Threatened Area), ReSeDa (Remote Sensing Data Assimilation), Yaqui'08, HAPEX-Sahel (Hydrology-Atmosphere Pilot Experiment), IHOP (International H2O Project), Monsoon'90 and the Southern Great Plains 1997 (SGP'97) experiment (references are provided in Table 1). Among the 34 sites, 26 are located in agricultural fields (BELon, CHOe2, DEGeb, DEKli, DESeh, DKVou, ESEFE, ESES2, FRAur, FRAvi, FRGri, FRLam, FRRe1, FRRe2, IECa1, ITBCi, ITCas, ITRo4, MOSR1, MOSR2, MEYaq, NIMil, USArm, USIb1, USIHO, USSGP) and the rest over uncropped lands. The natural lands include sand desert (NIHAP), savanna fallow (NISav) and degraded land (NIDeg) in Niger, native grass in Australia (AUStu), grass for silage or hay in the USA (USDk1), short grass following fireforest in the USA (USFwf), and sparse shrub in the USA (USMo1 and USMo7). As indicated in Table 1, the study sites cover a large range of surface conditions, with sand and clay fractions ranging from 0.05 to 0.92 and from 0.02 to 0.56, respectively.

The data collected at the above-selected sites contain sand and clay fractions, and the following surface variables measured at the hourly or subhourly time scale: near-surface soil moisture θ, latent heat flux LE, sensible heat flux H, net radiation Rn, ground conduction G, and meteorological forcing composed of air temperature T_a, wind speed u_a, solar radiation R_g and air relative humidity h_a at a reference height (typically 2 m). For the sites where a direct measurement of LE is unavailable, latent heat flux is estimated as the residual of the energy balance equation. For the sites where the four flux components (LE, H, Rn, G) are available, H and LE are systematically corrected using the Bowen ratio method [*Twine et al.*, 2000]. Note that θ is generally measured at around 5 cm depth but it is located at a shallower or deeper depth at few sites (see Table 1). The "observed" SEE is derived from the ratio of observed evaporation to the potential evaporation, defined as the evaporation based on equation (2) with no surface resistance ($r_{ss} = 0$) but using other observed variables (Rn,G,T_a,u_a,h_a).

One key aspect in this analysis is the identification of the periods when the sites can be considered as under "bare soil" conditions. In this study, a "bare soil" period is defined as a period of time when the plant transpiration is either negligible or small compared to soil evaporation. Hence the term "bare soil" includes both actual bare soil conditions, and soils partially covered by mulch, crop residue, or sparse vegetation. Whereas it is difficult to quantitatively assess the relative weight of evaporation and transpiration without any direct measurement of the evaporation/transpiration partitioning [*Wang et al*., 2014], some indirect indicators can be used like the Leaf Area Index (LAI), or in-field knowledge of agricultural practices like sowing, tillage and harvest. The bare soil periods were extracted with as much accuracy as possible.

Several sites (ESEFE, NIHAP, USIHO, USSGP) have been monitored under real bare soil conditions in the frame of short-term intensive field campaigns. Most of the sites though are equipped with long-term flux stations located in agricultural fields for which the sowing, tillage and harvest dates have been recorded across one or several growing seasons. Precise and multiannual field work information are available for 14 sites of the European flux database and 3 sites of the Ameriflux database (including all the other variables required in this analysis). In practice, the soil is assumed to be approximately bare during 20 days after each tillage, sowing or harvest date. In this paper, no distinction is made between the bare soil periods following tillage, sowing and harvest. Such additional information might be used in future studies to help separate the effect of soil roughness (after tillage) and the presence of crop residue (after harvest) on the soil evaporation process. Different strategies have been adopted regarding the uncropped lands. The grassland site AUStu is assumed to be bare when the satellite-derived vegetation index is minimum. The savanna fallow NISav is assumed to be bare from the beginning of the Niger 2006 experiment until grass started growing following the first monsoon rainfall events. The grassland site USDk1 is assumed to be bare during 20 days after the annual or biannual harvest date. The sparsely vegetated grassland USFwf, the degraded land NIDeg, and shrublands USMo1 and USMo7 are assumed to be approximately bare at all time (when flux measurements are available).

3. Three Common Evaporation Models

The evaporation modules of three common land-surface schemes are described below. The soil evaporation module of H-TESSEL was recently updated in *Albergel et al*. [2012]. The soil resistance is expressed as:

$$r_{ss}=\frac{\theta_{fc}-\theta_{res}}{\theta-\theta_{res}}\times r_{ss,min} \text{ for } \theta > \theta_{res} \tag{8}$$

with $r_{ss,min}$ (s m^{-1}) being the minimum soil resistance (set to 50 s m^{-1}) [*ECMWF*, 2014], θ_{fc} (m^3 m^{-3}) the soil moisture at field capacity, and θ_{res} (m^3 m^{-3}) the residual soil moisture.

The soil evaporation module of ISBA is based on the α method [*Noilhan and Planton*, 1989]. It represents the nonlinear behavior of α as:

$$\alpha=\begin{cases} 0.5-0.5\cos\left(\pi\theta/\theta_{fc}\right), & \text{if } \theta \leq \theta_{fc} \\ 1, & \text{if } \theta > \theta_{fc} \end{cases} \tag{9}$$

Regarding CLM, the soil evaporation module of the former version 3.5 [*Oleson et al*., 2007] was based on both α and r_{ss} methods as in equation (6). The water activity α was obtained using the Kelvin equation [*Philip and de Vries*, 1957]:

$$\alpha=\exp\left[\psi g/(1\times10^3 R_{wv}T)\right] \tag{10}$$

with g (m s^{-2}) being the gravitational constant, R_{wv} (J kg^{-1} K^{-1}) the gas constant for water vapor, and ψ (mm) the soil water matric potential of the surface soil layer computed as:

$$\psi=\psi_{sat}\times(\theta/\theta_{sat})^{-b_{CH}} \tag{11}$$

with ψ_{sat} (mm) being the air entry pressure, θ_{sat} (m^3 m^{-3}) the soil moisture at saturation, and b_{CH} the Clapp and Hornberger parameter [*Clapp and Hornberger*, 1978]. r_{ss} was derived from *Passerat de Silans* [1986] and *Sellers et al*. [1992]:

$$r_{ss}=\exp\left(A-B\,\theta/\theta_{fc}\right) \tag{12}$$

with A and B being two best-fit parameters estimated as 8.206 and 4.255 respectively using FIFE'87 measurements in *Sellers et al*. [1992]. Despite its empirical nature, the modeling approach of *Passerat de Silans*

[1986] has been widely used in land-surface models [*Sellers et al*., 1992, 1996; *Kustas et al*., 1998; *Vidale and Stöckli*, 2005; *Gentine et al*., 2007; *Crow et al*., 2008; *Oleson et al*., 2008; *Stöckli et al*., 2008]. The r_{ss} formulation in equation (12) is referred to as S92 in the following.

The soil evaporation module of the last (4.5) CLM version [*Oleson et al*., 2013] combines both α and β methods as in equation (7). α is estimated as in equation (10) and β is expressed as in *Lee and Pielke* [1992]:

$$\beta=\begin{cases} [0.5-0.5\cos(\pi\theta/\theta_{fc})]^2, & \text{if } \theta \le \theta_{fc} \\ 1, & \text{if } \theta > \theta_{fc} \text{if } \alpha e_{sat}(T) < e_a \end{cases} \tag{13}$$

The pedotransfer functions (PTFs) used to estimate θ_{fc}, θ_{res}, ψ_{sat}, θ_{sat}, and b_{CH} from sand and clay fractions are presented in Appendix A.

4. A Downward Modeling Approach of SEE

The rationale for choosing to model SEE instead of soil evaporation directly is that SEE, as a normalized variable, helps disentangle the two main factors controlling soil evaporation: evaporative demand (or *LEp*) and soil water availability. In particular, the SEE fosters the decoupling between the evaporation cycles associated with (1) the diurnal, seasonal and climatic variations of *LEp* and (2) the variations of soil water availability due to natural (rainfall) and/or man-induced (irrigation) precipitations. Note that the formulation in SEE only partly decouples the effect of soil water availability and *LEp* since the soil moisture profile changes with *LEp* [*Merlin et al*., 2011], and *LE* and *LEp* are generally coupled (e.g., see complementary relationship in *Lintner et al*. 2015]. Moreover, the advective part also contributes to SEE due to the drop in temperature that reduces Cw at the evaporative surface [*Chanzy and Bruckler*, 1993]. Nonetheless, the normalization of actual evaporation by the evaporative demand removes the first order effect of *LEp* on *LE*, and sets SEE to lie between $\sim$0 and 1. The limits are theoretically reached when soil water availability is respectively negligible ($\theta=\theta_{res}$, SEE $\sim$ 0) and maximum ($\theta=\theta_{sat}$, SEE=1) regardless of the atmospheric evaporative demand. Soil evaporation can then be estimated by multiplying the modeled SEE by *LEp*, which is derived from meteorological data solely.

Another significant advantage of the formulation in SEE is the strong link with remote sensing variables available in the thermal and microwave frequencies. In particular, the SEE-based representation of evaporation is fully consistent with both the thermal-derived *T* normalized by wet/dry *T* endmembers [e.g., *Nishida et al*., 2003; *Stefan et al*., 2015], and the θ retrieved from microwave data [e.g., *Prévot et al*., 1984; *Simmonds and Burke*, 1999; *Zribi et al*., 2011].

A new SEE model is developed based on a downward (data-driven) approach. The downward modeling approach aims to minimize the number of model parameters while ensuring a sufficient flexibility of the SEE formulation to cover a large range of soil and atmospheric conditions. In practice, the step-wise procedure below is followed:

1. SEE is expressed based on equation (12), as a function of two parameters noted $r_{ss,ref}=\exp(A)$ and $\theta_{efolding}=\theta_{fc}/B$,
2. $r_{ss,ref}$ and $\theta_{efolding}$ are analytically expressed as a function of meteorological conditions, and of two observational parameters namely the cut-off soil moisture value $\theta_{1/2}$ (m^3m^{-3}) at which SEE=0.5, and the first derivative noted $\Delta\theta_{1/2}^{-1}$ (m^3m^{-3}) of SEE at $\theta_{1/2}$,
3. SEE is assumed to be a unique function of θ, $\theta_{1/2}$ and $\Delta\theta_{1/2}^{-1}$. The variabilities of SEE attributed to factors other than θ (e.g., soil texture) are therefore contained in $\theta_{1/2}$ and $\Delta\theta_{1/2}^{-1}$,
4. a retrieval procedure of $\theta_{1/2}$ and $\Delta\theta_{1/2}^{-1}$ is proposed for a given time series of SEE and θ data (the calibration period should include significant variability in θ i.e., at least one drying sequence),
5. variabilities in $\theta_{1/2}$ and $\Delta\theta_{1/2}^{-1}$ are interpreted in terms of soil and atmospheric conditions, which can be characterized by the soil texture, soil roughness, presence of stubble or mulch at the soil surface, shrinkage cracks, etc. In this study, a focus is made on a texture-based calibration of $\theta_{1/2}$ and $\Delta\theta_{1/2}^{-1}$ because sand and clay fractions are relatively easy to obtain and are generally available at the site level.

The input/output data sets and the main steps of the modeling, calibration and validation approaches are presented in the diagram of Figure 1. An analytical relationship between $(r_{ss,ref};\theta_{efolding})$ and $(\theta_{1/2};\Delta\theta_{1/2}^{-1})$ is first built by running a soil energy balance model for two extreme conditions with $r_{ss}=0$ and $r_{ss}\sim\infty$ using

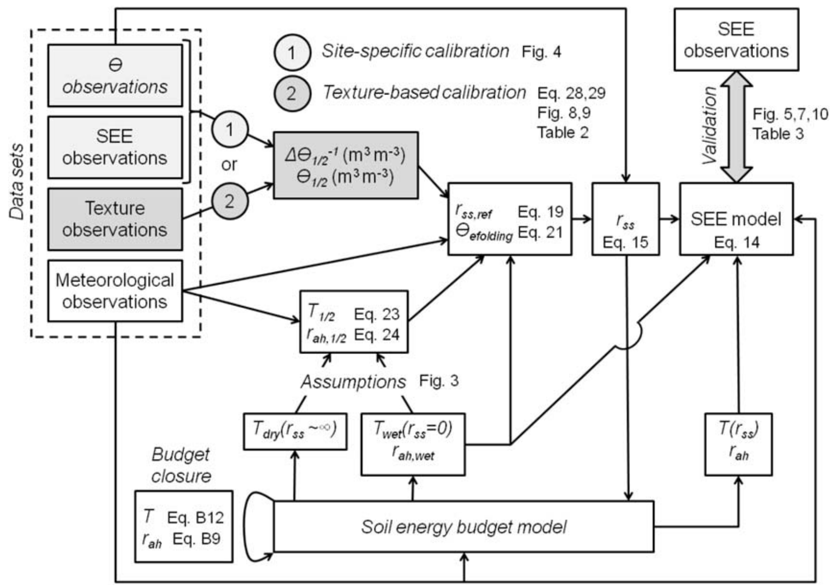

Figure 1. Overview of the modeling, calibration and validation approaches including input/output data sets and the main equations, figures and tables.

meteorological forcing solely, and by approaching the middle point from the two (wet and dry) reference points. Two methods are then investigated to estimate the pair $(\theta_{1/2}; \Delta\theta_{1/2}^{-1})$. The first method (site-specific calibration) is based on the time series of SEE and θ data for a given site, while the second method (texture-based calibration) parameterizes $\theta_{1/2}$ and $\Delta\theta_{1/2}^{-1}$ as a function of the clay and/or sand fractions for all sites. The associated equations, figures and tables are also indicated in the diagram for clarity. The model development is described below, along with the underlying assumptions.

4.1. r_{ss}-Based SEE Model

The energy balance of physically based land-surface schemes is generally represented using a resistance network. Therefore, the r_{ss}-based formulation is preferred, as it facilitates the integration of the SEE model in the majority of existing land-surface models. SEE is hence written as:

$$\mathrm{SEE} = \frac{e_{sat}(T) - e_a}{e_{sat}(T_{wet}) - e_a} \times \frac{r_{ah,wet}}{r_{ss} + r_{ah}} \tag{14}$$

with T_{wet} being the temperature of a water-saturated soil (corresponding to $r_{ss} = 0$), and $r_{ah,wet}$ the associated aerodynamic resistance to heat transfer. Note that in the prospect of integrating the above formulation in a given land-surface model, equation (14) can be inverted to express r_{ss} as a function of modeled SEE.

In equation (14), the variability of SEE attributed to soil water availability (via θ and the soil properties including soil texture, structure, and roughness) is assumed to be contained in r_{ss}. In this study, the general form of the S92 r_{ss} formulation is used:

$$r_{ss} = r_{ss,ref} \exp(-\theta/\theta_{efolding}) \tag{15}$$

with $r_{ss,ref} = \exp(A)$ (s m^{-1}) being the asymptotic value of r_{ss} for $\theta \sim 0$, and $\theta_{efolding} = \theta_{fc}/B$ (m^3 m^{-3}) the soil moisture value at which $r_{ss} = r_{ss,ref}/e$. The exponential form of equation (15) is convenient for analytically expressing the derivatives of r_{ss} and SEE.

4.2. Linear Approximation of SEE at the Mid-Value

Many studies have documented the strongly nonlinear behavior of SEE as a function of θ [e.g., *Chanzy and Bruckler*, 1993; *Komatsu*, 2003; *Merlin et al.*, 2011]. Modeling a nonlinear phenomenon is challenging because small uncertainties in model parameterization may have a large impact on predictions. As an attempt to approximate SEE over its full range $[0-1]$, SEE is approached linearly at the mid-value (0.5). The linear approximation of SEE(θ) at SEE=0.5 sets two constraints on the model. First, the soil moisture value at which SEE=0.5 is noted $\theta_{1/2}$:

$$\text{SEE}(\theta_{1/2})=0.5 \tag{16}$$

Second, the first derivative of SEE at $\theta_{1/2}$ is set to the slope ($\Delta\theta_{1/2}^{-1}$) of the linear regression between SEE and θ observations:

$$\left(\frac{\partial \text{SEE}}{\partial \theta}\right)(\theta_{1/2})=\Delta\theta_{1/2}^{-1} \tag{17}$$

The combination of the above two equations allows to estimate both $r_{ss,ref}$ and $\theta_{efolding}$ parameters given a time series of SEE and θ observations (described in the following section). As an illustration of the approximation approach, Figure 2 plots the SEE simulated by the model in *Merlin et al*. [2011] as a function of θ for two different sets of parameters. In *Merlin et al*. [2011], SEE was written as:

$$\text{SEE}=\begin{cases}[0.5-0.5\cos(\pi\theta/\theta_{sat})]^P, & \text{if } \theta \le \theta_{sat} \\ 1, & \text{if } \theta > \theta_{sat}\end{cases} \tag{18}$$

with P being a semi-empirical parameter expressed as a function of the soil moisture sensing depth (L) and LEp. The phenomenological expression in equation (18) is based on the observation that both L and LEp have an equivalent impact on SEE, meaning that (1) SEE is controlled by the soil moisture profile within the soil thickness L and (2) the soil moisture profile is affected by both L and LEp. This is consistent with the recent study of *Brutsaert* [2014] who described the daily water flow in the soil profile by considering the soil as an infinite domain during stage 1, and a layer of constant thickness whose lower boundary is a zero-flux plane during stage 2. The decrease of SEE with increasing LEp is generally related to the formation of a dry surface layer above the evaporative front [*Fritton et al*., 1967; *Yamanaka et al*., 1998], modifying the soil moisture profile within the soil sensing depth. Figure 2 plots the SEE simulated with $(P_1,\theta_{sat,1})=(1,0.40)$ and $(P_2,\theta_{sat,2})=(4,0.45)$. One observes that $\theta_{1/2}$ and $\Delta\theta_{1/2}^{-1}$ are different in both cases. The modeling strategy aims to represent the nonlinear behavior of SEE within the full SEE range from $\theta_{1/2}$ and $\Delta\theta_{1/2}^{-1}$ parameters, and the exponential formulation in equation (15).

4.3. Analytical Expressions of $r_{ss,ref}$ and $\theta_{efolding}$

Parameters $r_{ss,ref}$ and $\theta_{efolding}$ in equation (15) are analytically expressed as a function of $\theta_{1/2}$, $\Delta\theta_{1/2}^{-1}$, soil temperature (T_{wet} and $T_{1/2}$) and aerodynamic resistance ($r_{ah,wet}$ and $r_{ah,1/2}$) values corresponding to $r_{ss}=0$ and $\theta=\theta_{1/2}$, respectively. A soil energy balance model [e.g., *Norman et al*., 1995; *Merlin and Chehbouni*, 2004] is used to estimate both pairs $(T_{wet}, r_{ah,wet})$ and $(T_{1/2}, r_{ah,1/2})$ for a given meteorological forcing.

Briefly, $r_{ss,ref}$ is derived by inverting equation (15):

$$r_{ss,ref}=r_{ss,1/2}\exp(\theta_{1/2}/\theta_{efolding}) \tag{19}$$

with $r_{ss,1/2}$ being the soil resistance at $\theta_{1/2}$ obtained by combining equations (14) and (16):

$$r_{ss,1/2}=2\frac{e_{sat}(T_{1/2})-e_a}{e_{sat}(T_{wet})-e_a}r_{ah,wet}-r_{ah,1/2} \tag{20}$$

$\theta_{efolding}$ is obtained by applying the first derivative at $\theta=\theta_{1/2}$ to the soil energy balance equation:

$$\theta_{efolding}=\frac{\frac{r_{ss,1/2}}{r_{ss,1/2}+r_{ah,1/2}}(e_{sat}(T_{1/2})-e_a)+f(\theta_{1/2})\dot{e}_{sat}(T_{1/2})}{\frac{r_{ss,1/2}+r_{ah,1/2}}{r_{ah,wet}}(e_{sat}(T_{wet})-e_a)}\times\frac{1}{\Delta\theta_{1/2}^{-1}} \tag{21}$$

with $\dot{e}_{sat}$ being the derivative of saturated vapor pressure with respect to T and $f(\theta_{1/2})$ expressed as:

$$f(\theta_{1/2})=-\frac{\frac{r_{ss,1/2}r_{ah,1/2}}{(r_{ss,1/2}+r_{ah,1/2})^2}(e_{sat}(T_{1/2})-e_a)}{\gamma+\frac{r_{ah,1/2}}{r_{ss,1/2}+r_{ah,1/2}}\dot{e}_{sat}(T_{1/2})+4\frac{\gamma}{\rho C_P}\epsilon\sigma(1-C_G)T_{1/2}^3 r_{ah,1/2}} \tag{22}$$

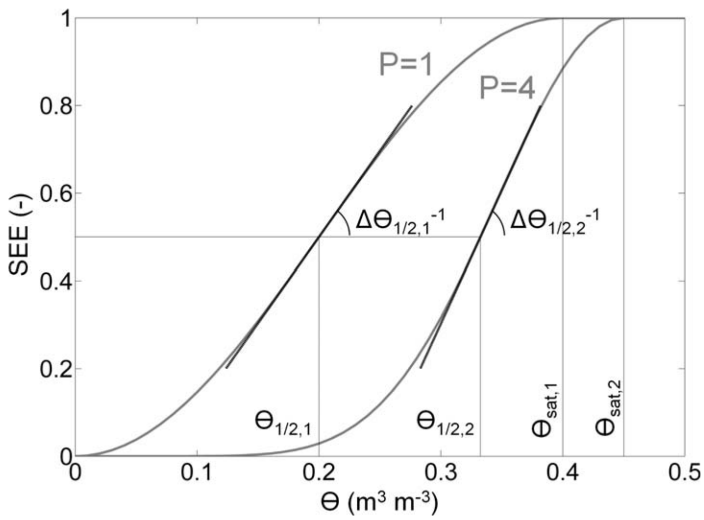

Figure 2. The SEE(θ) relationship is approximated at the midvalue (SEE=0.5) by the tangent defined by the pair $(\theta_{1/2}, \Delta\theta_{1/2}^{-1})$, for two different scenarios 1 and 2.

with C_G being the ratio of the ground conduction to soil net radiation. A presentation of the soil energy balance model is provided in Appendix B and the analytical development of $\theta_{efolding}$ is described in Appendix C.

4.4. Model Assumptions

In equations (20)–(22), a first guess of $T_{1/2}$ is given by:

$$T_{1/2}=(T_{wet}+T_{dry})/2 \tag{23}$$

with T_{dry} being the T of a fully dry soil (corresponding to $r_{ss}\sim\infty$), and a first guess of $r_{ah,1/2}$ is given by:

$$r_{ah,1/2}=r_{ah}(T_{1/2}) \tag{24}$$

with $r_{ah}(T_{1/2})$ being the aerodynamic resistance estimated using the Richardson number (see equations (B9) and (B11)) for atmospheric stability corrections at $T=T_{1/2}$. Note that equations (23) and (24) are approximations since an accurate determination of $T_{1/2}$ and $r_{ah,1/2}$ would require an iterative process on $r_{ss,1/2}$ (and $r_{ss,ref}$ and $\theta_{efolding}$), and thus multiple applications of the soil energy balance model. However, such approximations are considered to be valid at first order given that turbulent heat fluxes and surface temperatures are near linearly related [e.g., *Moran et al*., 1994; *Roerink et al*., 2000; *Merlin*, 2013].

To assess the validity of the model assumptions, Figures 3b, 3e, and 3h compare the SEE simulated by the S92 and new r_{ss} formulations as a function of observed θ, for NIMil, FRAvi and FRLam data sets, respectively. In general, the scatter in simulated SEE is reduced with the new formulation. This is consistent with the assumed number (3) of degrees of freedom of the SEE model expressed as a function of θ, $\theta_{1/2}$ and $\Delta\theta_{1/2}^{-1}$ solely. Moreover, the behavior at around $\theta=\theta_{1/2}$ of the SEE simulated using the new r_{ss} formulation is very close to the mean regression defined by the pair $(\theta_{1/2}, \Delta\theta_{1/2}^{-1})$. The linearity assumption SEE(T) implicitly made in equation (23) can also be verified by investigating the relationship between simulated SEE and the simulated temperature T normalized by T_{dry} and T_{wet}:

$$T_{norm}=\frac{T_{dry}-T}{T_{dry}-T_{wet}} \tag{25}$$

Figures 3c, 3f, and 3i plot simulated SEE versus simulated T_{norm} for the S92 and new r_{ss} formulations separately, and for NIMil, FRAvi and FRLam data sets, respectively. The physically based soil energy balance model represents a quasi linear relationship between T_{norm} and SEE for all three data sets, regardless the r_{ss} formulation. Note that T_{norm} slightly overestimates simulated SEE, especially at the mid values. This is due to the impact of the dependence of r_{ah} on $T-T_a$ (see equation (B11)) on modeled SEE. However, the mean bias between T_{norm} and simulated SEE is very small in all cases. The above verifications thus indicate that the assumptions in equations (23) and (24) are deemed acceptable to approximate SEE at its mid value.

4.5. Retrieving $\theta_{1/2}$ and $\Delta\theta_{1/2}^{-1}$ from SEE and θ Data

An algorithm is proposed to retrieve both $\theta_{1/2}$ and $\Delta\theta_{1/2}^{-1}$ from a given time series of SEE and θ observations. The retrieval of $\theta_{1/2}$ and $\Delta\theta_{1/2}^{-1}$ is not a trivial task due to 1) the nonlinear behavior of SEE(θ), 2) uncertainties in SEE and θ observations, and 3) as mentioned before the possible impact of variability factors other than θ, such as the sensing depth of θ measurements, soil moisture profile, soil roughness, presence of stubble or mulch at the soil surface, shrinkage cracks, etc., which may significantly affect the observed relationship between SEE and θ. Nonetheless, the procedure described below is designed to provide a robust estimate of $\theta_{1/2}$ and $\Delta\theta_{1/2}^{-1}$ for strongly noised and nonlinear SEE(θ) relationships.

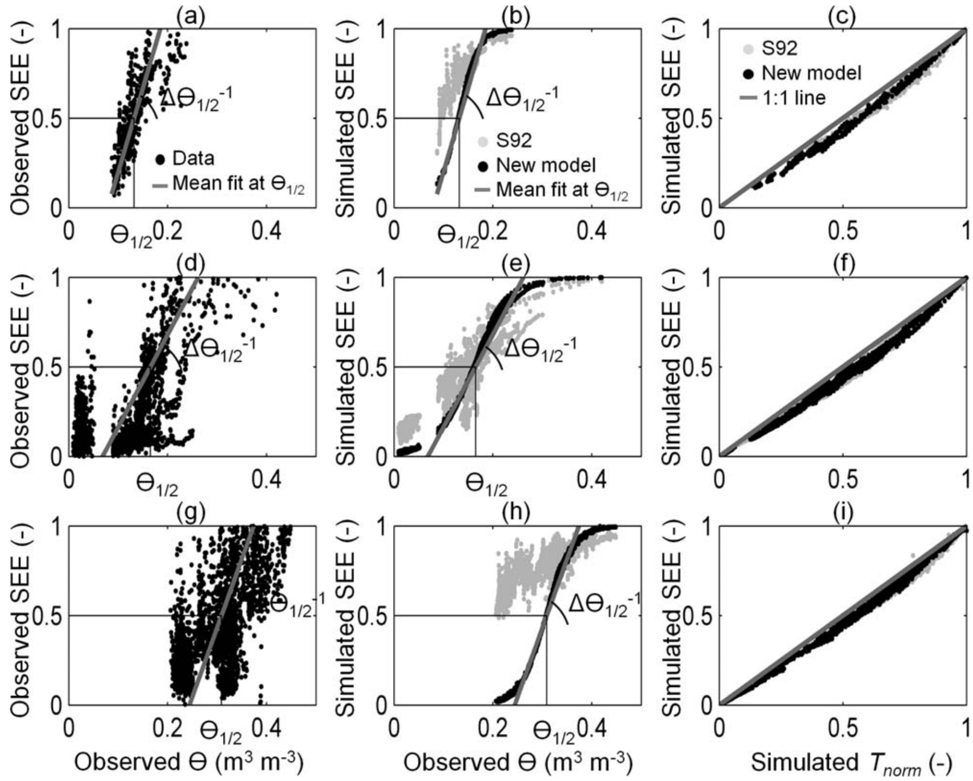

Figure 3. (left) Observed SEE versus observed θ, (middle) simulated SEE versus observed θ, and (right) simulated SEE versus simulated T_{norm}, ranging from sandy to clayey soil conditions: (top) NIMil, (middle) FRAvi, and (bottom) FRLam data set.

The main idea is to consider a regression between SEE and θ around $\theta=\theta_{1/2}$. A schematic representation based on the AUStu data set is provided in Figure 4. First, the full SEE range $[0-1]$ is split into 20 0.05-wide bins, and the SEE and θ values falling into each SEE bin are averaged separately to provide a pair $(\overline{\mathrm{SEE}}_k, \bar{\theta}_k)$ per bin. Then, 10 regression segments are computed by joining the two points $(\overline{\mathrm{SEE}}_k, \bar{\theta}_k)$ and $(\overline{\mathrm{SEE}}_{k+10}, \bar{\theta}_{k+10})$ for $k=1,\ldots,10$. Next, the slope $(\Delta\theta_{1/2}^{-1})$ of the mean regression at around the mid-value (SEE=0.5) is estimated by taking the average of the slope of the 10 distinct regression segments, weighted by the number of data points within each bin pair (i.e., weights are computed as the multiplication of the number of data points within the two bins k and $k+10$). Last, $\theta_{1/2}$ is derived from $\Delta\theta_{1/2}^{-1}$ and the mean observed θ. Note that the average of multiple slopes is more appropriate than using a single slope centered on SEE=0.5 as it allows for a robust application to any data set, including those with observed θ values mostly in the lower or higher soil moisture range.

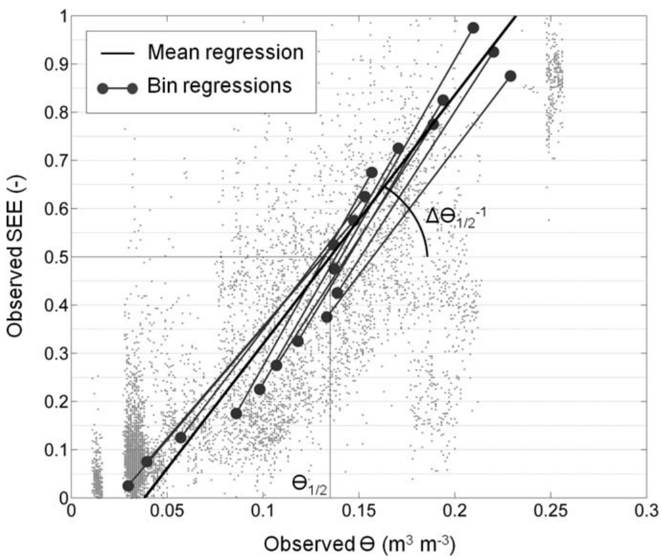

Figure 4. Schematic representation of the retrieval of $\theta_{1/2}$ and $\Delta\theta_{1/2}^{-1}$ from the AUStu data set.

As an illustration, Figures 3a, 3d, and 3g plot observed SEE versus observed

10.1002/2015WR018233

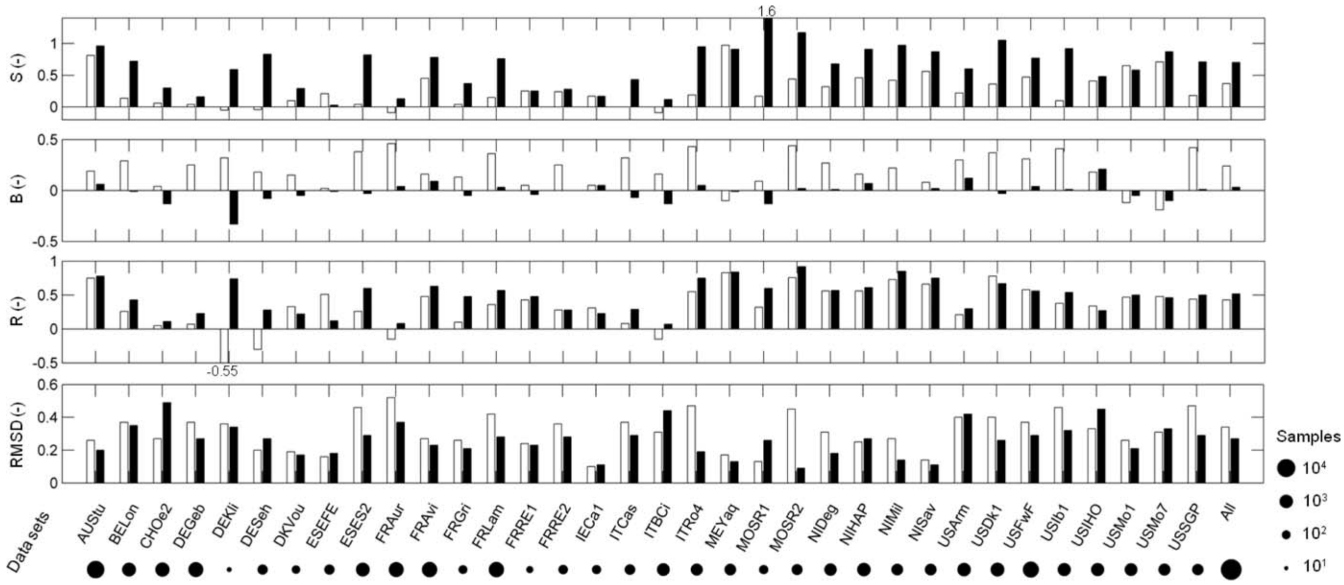

Figure 5. Bar graph of the root mean square difference (RMSD), correlation coefficient (R), mean bias (B), and slope of the linear regression (S) between simulated and observed SEE for the new r_{ss} with site-specific $\theta_{1/2}$ and $\Delta\theta_{1/2}^{-1}$ parameters (black) and for the S92 r_{ss} (white). The number of data samples for each site is also illustrated.

θ for NIMil, FRAvi and FRLam data sets respectively, ranging from sandy to clayey soil conditions. The retrieved $\theta_{1/2}$ and $\Delta\theta_{1/2}^{-1}$ significantly vary across the three sites.

5. Evaluation and Intercomparison of SEE Models

In this section, the SEE model based on the $r_{ss}(\theta_{1/2}, \Delta\theta_{1/2}^{-1})$ formulation is evaluated using the bare soil data collected at the 34 sites. First, $\theta_{1/2}$ and $\Delta\theta_{1/2}^{-1}$ are retrieved for each data set, and the new r_{ss} formulation is assessed using site-specific parameters. Second, a generic parameterization of $(\theta_{1/2}, \Delta\theta_{1/2}^{-1})$ is proposed as a function of soil texture i.e., the clay and sand percentages. Third, the texture-based r_{ss} formulation is compared with the PTFs of four common evaporation models in terms of SEE estimates. Note that only the data with $Rn-G > 100$ W m^{-2} and $LEp > 100$ W m^{-2} are considered in this study to avoid large uncertainties in SEE observations and to avoid energy limited conditions. The C_G coefficient in equation (22) is set to the minimum between 0.315 [*Kustas et al.*, 1991] and the observed G to Rn ratio, and the C_G values below 0.05 are set to 0.05 according to maximum and minimum values found in the literature [*Su*, 2002].

5.1. Site-Specific Calibration

The pair $(\theta_{1/2}, \Delta\theta_{1/2}^{-1})$ is retrieved using the algorithm described in section 4.5 for each site separately. To assess the impact of a site-specific calibration of $r_{ss,ref}$ and $\theta_{efolding}$, SEE simulations are evaluated against multi-site observations. Moreover, results are compared with the SEE simulated by the S92 rss formulation. Figure 5 presents bar graphs of the root mean square difference (RMSD), mean bias (B), correlation coefficient (R) and slope of the linear regression (S) between simulated and observed SEE in both cases, and the number of data samples for each site separately. The mean (weighted by the number of data samples per site) RMSD is 0.27 instead of 0.34, the mean R is 0.52 instead of 0.43, the mean B is 0.03 instead of 0.24, and the mean S is 0.70 instead of 0.37 for the calibrated new and S92 formulations, respectively. Statistics are generally improved with the calibrated rss formulation. Especially, the mean bias is much reduced and the slope of linear fit closer to 1. The strategy of approximating SEE at $(\theta_{1/2}, 0.5)$ thus appears to be effective in improving the representation of SEE over its full range. Note that a sensitivity analysis (not shown) revealed that setting C_G to a constant between 0.25 and 0.40 degrades the modeling results especially in terms of correlation and slope of the linear regression between modeled and observed SEE.

When looking at individual sites in Figure 5, a degradation of RMSD, R and S can be observed. Notably the statistics for CHOe2, ITBCi, and USIHO, and to a lesser extent for ESEFE and IECa1 indicate an increase of the RMSD with the calibrated new (compared to S92) rss formulation. To help interpret those seemingly

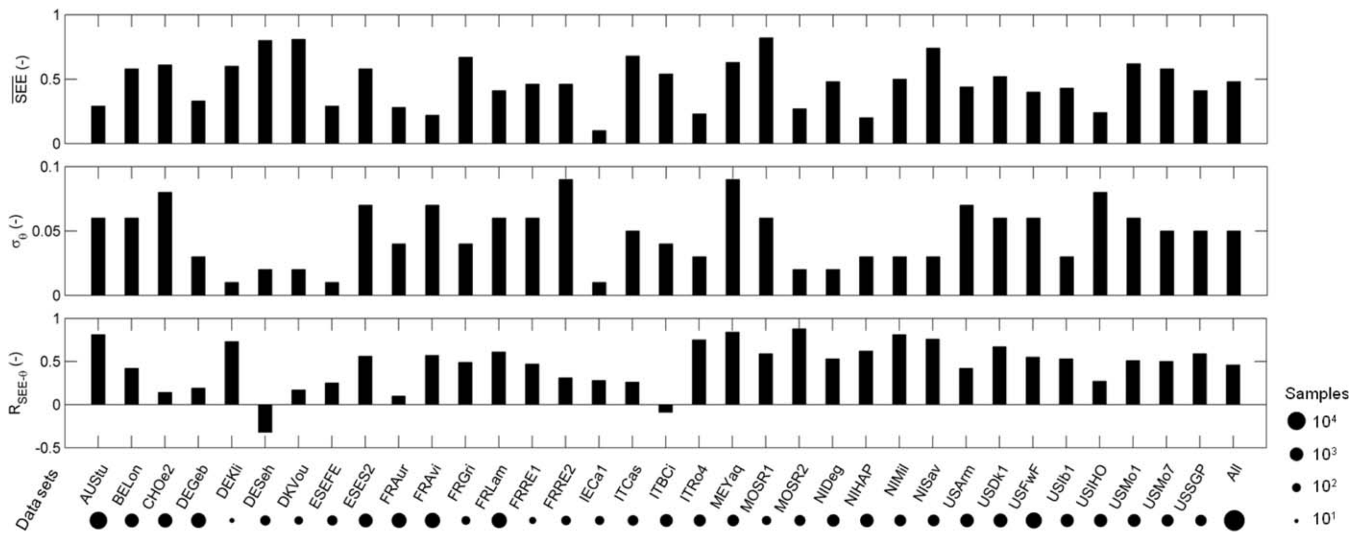

Figure 6. Bar graph of the mean observed SEE ($\overline{SEE}$), standard deviation of observed θ (σ_θ), and correlation coefficient between observed SEE and observed θ ($R_{SEE-\theta}$). The number of data samples for each site is also illustrated.

inconsistent results, Figure 6 presents bar graphs of the mean observed SEE ($\overline{SEE}$), the standard deviation of observed θ (σ_θ), the correlation coefficient between SEE and θ observations ($R_{SEE-\theta}$) and the number of data samples (n) for each site separately. The correlation coefficient between SEE and θ observations is poor with 0.14, -0.09, and 0.27 for CHOe2, ITBCi, and USIHO respectively, while the mean $R_{SEE-\theta}$ for all sites is estimated as 0.46. In addition σ_θ for ESEFE and IECa1 is very small (0.01) as compared with the mean σ_θ (0.05) for all sites, and the $\overline{SEE}$ for ESEFE, IECa1 and USIHO (0.29, 0.10 and 0.24 respectively) is relatively far from the SEE mid value, as compared with the mean $\overline{SEE}$ (0.48) for all sites. Hence the poorer SEE statistics for CHOe2, ESEFE, IECa1, ITBCi and USIHO are probably attributed to the limited range of soil moisture and atmospheric conditions present in the respective data sets. A lack of variability in the surface conditions encountered in the input data set weakens the robustness of the retrieval approach.

Figure 7 plots the SEE simulated using the site-specific $(\theta_{1/2}, \Delta\theta_{1/2}^{-1})$ as a function of observed SEE for different ranges of clay fractions separately. When comparing the RMSD, R, B and S for each clay fraction range, one observes that the performance of the SEE model is superior for low clay contents ($f_{clay} < 0.20$) than for relatively high clay content ($f_{clay} \geq 0.30$). The effect is especially reflected in R and S, which both are about

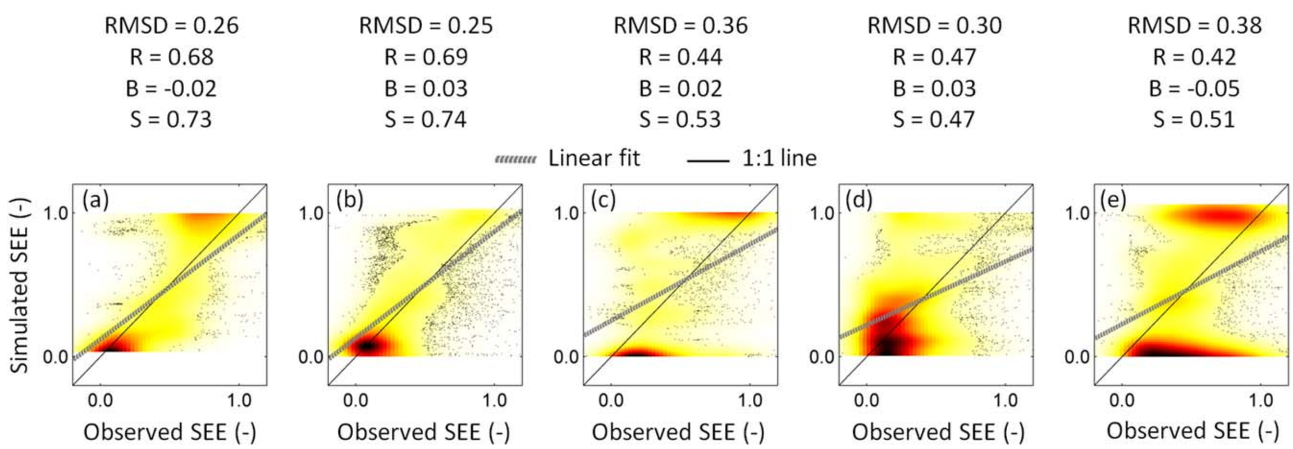

Figure 7. The SEE simulated by the new r_{ss} model with site-specific calibration is plotted as a function of observed SEE for different ranges of clay fraction: (a) $f_{clay} < 0.10$, (b) $0.10 \leq f_{clay} < 0.20$, (c) $0.20 \leq f_{clay} < 0.30$, (d) $0.30 \leq f_{clay} < 0.40$, and (e) $f_{clay} \geq 0.40$. Each graph is a smoothed histogram of the bivariate (modeled versus observed) SEE data. Black shading represents the maximum smoothed density of data points, while the individual points (ouliers) are plotted where the smoothed density is less than 10% of the maximum density. The root mean square difference (RMSD), correlation coefficient (R), mean bias (B), and slope of the linear regression (S) between simulated and observed SEE are also indicated for each case.

Table 2. Slope and Intercept of the Linear Regression, and Correlation Coefficient Between Retrieved $\theta_{1/2}$ and Clay and Sand Fractions, Respectively for Site Data Sets Containing at Least 1, 101, and 501 Samples, Separately

	Clay-Based Linear Fit			Sand-Based Linear Fit		
n	Slope (m^3 m^{-3})	Intercept (m^3 m^{-3})	R	Slope (m^3 m^{-3})	Intercept (m^3 m^{-3})	R
> 0	0.41	0.11	0.62	−0.26	0.29	−0.65
> 100	0.41	0.11	0.57	−0.26	0.29	−0.69
> 500	0.43	0.10	0.76	−0.27	0.29	−0.76

0.70 and 0.45, for the $f_{clay} < 0.20$ and $f_{clay} \geq 0.30$ case respectively. It is suggested that SEE is more difficult to model from θ data in clayey than in sandy soils, especially because of the "dynamic" formation of a dry surface layer under relatively large evaporative demand conditions [*Fritton et al.*, 1967; *Yamanaka et al.*, 1998]. Nevertheless, the "static" site-specific calibration of r_{ss} via $\theta_{1/2}$ and $\Delta\theta_{1/2}^{-1}$ (compared to the default S92 parameters) significantly reduces the bias between simulated and observed SEE for each clay fraction range, and generally improves the R, S and RMSD across the multi-site data set. This is the rationale for developing a texture-based calibration of $\theta_{1/2}$ and $\Delta\theta_{1/2}^{-1}$ as a first guess of the variabilities in the parameters $r_{ss,ref}$ and $\theta_{efolding}$.

5.2. Toward a Texture-Based Calibration

Given that $\theta_{1/2}$ and $\Delta\theta_{1/2}^{-1}$ are semi-empirical parameters, and that SEE and θ observations may not be available to retrieve the pair $(\theta_{1/2}, \Delta\theta_{1/2}^{-1})$ at all locations, a PTF is proposed. In practice, the parameters $\theta_{1/2}$ and $\Delta\theta_{1/2}^{-1}$ retrieved for each site separately are related to the site sand and clay fractions.

A significant correlation is found between retrieved $\theta_{1/2}$ and soil texture with a correlation coefficient in the range of 0.6–0.8 for both sand and clay fractions (see Table 2). Specifically, the R statistics estimated for sites with $n > 0$ (34 sites), $n > 100$ (30 sites) and $n > 500$ (19 sites) is 0.62, 0.57 and 0.76 with clay fraction, and −0.65, −0.69 and −0.76 with sand fraction, respectively. Figure 8 plots retrieved $\theta_{1/2}$ as a function of sand and clay fractions for the 19 sites with $n > 500$. The soil moisture $\theta_{1/2}$ at which SEE=0.5 is an increasing function of clay fraction and a decreasing function of sand fraction. This indicates that the hydric potential curves that control evaporation according to θ are shifted as a function of texture. The observed phenomenon is also consistent with Fick's law, predicting that evaporation is inversely proportional to porosity and depth of the vaporization front, which both increase with decreasing size of soil pores and particles [*Or et al.*, 2013]. Note that one site (ESES2) appears to significantly deviate from the linear regression based on either clay or sand fraction (see Figure 8). As a crop rice field, ESES2 is flooded most of the time. When

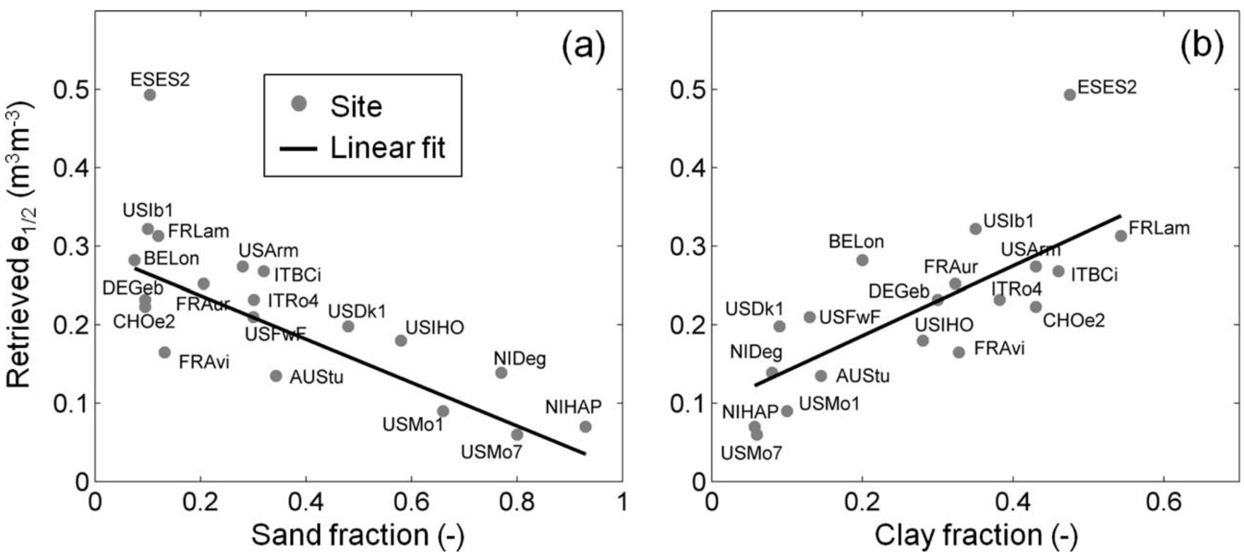

Figure 8. Semi-empirical parameter $\theta_{1/2}$ retrieved for each site separately, as function of (a) sand and (b) clay fraction for data sets containing at least 500 samples ($n > 500$), including the respective linear fits.

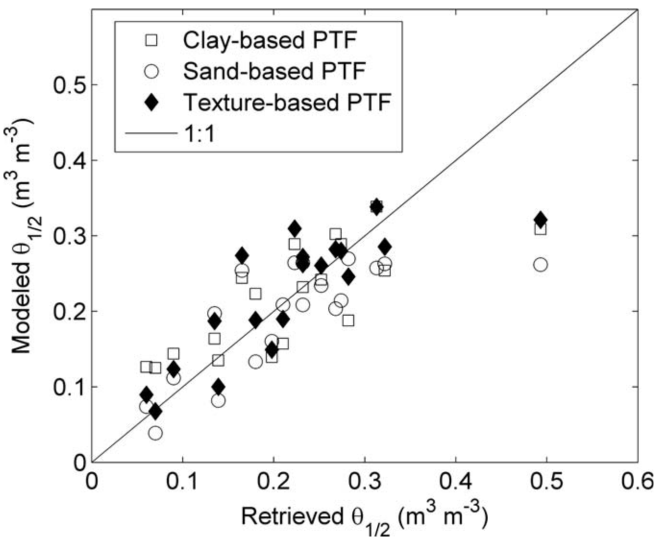

Figure 9. Modeled versus retrieved $\theta_{1/2}$ for clay-based, sand-based and texture-based (sand and clay together) PTF separately.

discarding the specific case of ESES2 from linear regressions, the R between retrieved $\theta_{1/2}$ and clay and sand fraction is 0.77 and -0.83, respectively. To quantify the consequences of site selection decisions, the 6 sparsely vegetated (AUStu, NISav, USDk1, USFwf, USMo1, USMo7) sites were removed from the "bare soil" database. The correlation between retrieved $\theta_{1/2}$ and clay/sand fraction decreased from 0.76 down to 0.69 (absolute value for $n>500$), indicating that site selection is a tradeoff between total number of points (including a range of clay/sand fractions) and potential quality.

Three PTFs of $\theta_{1/2}$ are tested, using the multi-site data set with $n>500$. The clay-based $\theta_{1/2}$ is:

$$\theta_{1/2}=0.10+0.43f_{clay} \tag{26}$$

and the sand-based model is:

$$\theta_{1/2}=0.29-0.27f_{sand}. \tag{27}$$

An interesting feature with the sand-based linear regression is that the extrapolated value of $\theta_{1/2}$ at $f_{sand}=1$ is ~ 0. A third PTF (in the following referred to as "texture-based PTF") is built from the multilinear regression of retrieved $\theta_{1/2}$ with both clay and sand fractions:

$$\theta_{1/2}=0.20+0.28f_{clay}-0.16f_{sand} \tag{28}$$

Figure 9 plots modeled versus retrieved $\theta_{1/2}$ for clay-based, sand-based and texture-based PTFs separately. The multilinear regression of $\theta_{1/2}$ including clay and sand fractions (texture-based PTF) improves the model statistics: the R (and RMSD) between modeled and retrieved $\theta_{1/2}$ is 0.76, 0.76 and 0.81 (and 0.065, 0.068 and 0.058 $m^3\ m^{-3}$) respectively. Although clay and sand fractions are somewhat correlated via the silt fraction ($f_{clay}+f_{sand}=1-f_{silt}$ in inorganic soils), it is suggested that both fractions provide complementary information on soil water retention capacity, especially in the case where one of the fraction (f_{clay} or f_{sand}) is small. Consequently, the PTF in equation (28) is used in the following to estimate $\theta_{1/2}$ from site-specific textural information.

Regarding $\Delta\theta_{1/2}^{-1}$, no significant correlation is obtained with either clay or sand fraction. The R estimated for sites with $n>0$, $n>100$, and $n>500$ is 0.06, 0.10 and 0.23 with clay fraction, and -0.04, -0.13 and -0.19 with sand fraction, respectively. Consequently, $\Delta\theta_{1/2}^{-1}$ is set to a constant equal to the mean value for all sites with $n>500$:

$$\Delta\theta_{1/2}^{-1}=8\ m^3m^{-3} \tag{29}$$

Note that the standard deviation of $\Delta\theta_{1/2}^{-1}$ across the 19 sites is about 4, which is relatively large compared to the mean. The variability of $\Delta\theta_{1/2}^{-1}$ can be attributed to a number of factors such as the soil water availability in deeper soil layers, atmospheric conditions (at interannual, seasonal, daily and hourly time scales), surface state (roughness, presence of residus, etc.), and farming practices (e.g., ploughing) for crop sites during the selected bare soil periods. Although the mean $\Delta\theta_{1/2}^{-1}$ may not be representative for all sites, equation (29) is used in the following as a best first guess.

Figure 10 presents bar graphs of the RMSD, R, B and S between simulated and observed SEE for the new r_{ss} with texture-based $\theta_{1/2}$ (equation (28)) and $\Delta\theta_{1/2}^{-1}$ (equation (29)) as well as for the S92 r_{ss} formulation.

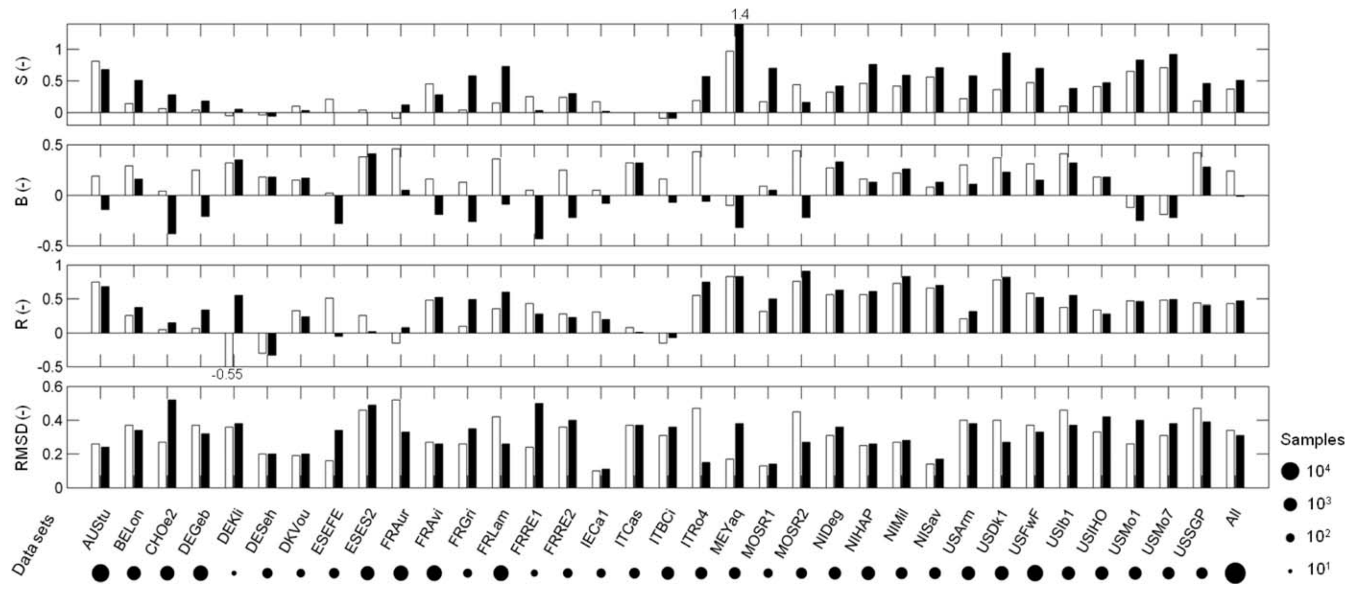

Figure 10. Same as for Figure 5 but for the new r_{ss} with $\theta_{1/2}$ estimated using the texture-based PTF and the mean $\Delta\theta_{1/2}^{-1}$ of all sites with $n > 500$.

Values are presented for each site separately, and additionally, the weighted mean (weighted by the number of data samples per site) is indicated. With respect to the latter, the RMSD is 0.31 instead of 0.34, R is 0.47 instead of 0.43, B is -0.01 instead of 0.24 and S is 0.51 instead of 0.37 for the texture-based new and S92 formulation, respectively. As in case of site-specific $\theta_{1/2}$ and $\Delta\theta_{1/2}^{-1}$ parameters (Figure 5), the new r_{ss} formulation outperforms the S92 r_{ss} formulation when using $\theta_{1/2}$ estimated by means of the texture-based PTF together with the mean $\Delta\theta_{1/2}^{-1}$ of all sites with $n > 500$. To assess the information provided by sand fraction and clay fraction separately and by multi-regressional use of the two in terms of SEE, metrics are also computed using the PTFs $\theta_{1/2}(f_{clay})$ in equation (26) and $\theta_{1/2}(f_{sand})$ in equation (27). The (weighted mean) RMSD is 0.32 and 0.34, R is 0.47 and 0.46, B is 0.03 and 0.05, and S is 0.52 and 0.49 for $\theta_{1/2}(f_{clay})$ and $\theta_{1/2}(f_{sand})$, respectively. Consistent with the assessment of the different PTFs per se, SEE estimations using PTFs based on either clay or sand fraction provide relatively similar results, while the PTF based on both $\theta_{1/2}(f_{clay}, f_{sand})$ in equation (28) still provides best SEE estimates.

5.3. Comparison With Common Evaporation Models

The PTFs of equations (28) and (29) are compared in terms of SEE estimates with the PTFs of four common evaporation models. Table 3 reports the RMSD, B, R and S between simulated and observed SEE for ISBA, H-TESSEL, and CLM (version 4.5) evaporation modules, and for S92 and new texture-based (texture-based $\theta_{1/2}$ and mean $\Delta\theta_{1/2}^{-1}$) r_{ss} formulations. In each case, statistics are provided for five different clay fraction ranges: $f_{clay} < 0.10$, $0.10 \leq f_{clay} < 0.20$, $0.20 \leq f_{clay} < 0.30$, $0.30 \leq f_{clay} < 0.40$ and $f_{clay} \geq 0.40$. The RMSD and B are systematically improved by the new r_{ss}. Among the five models, the minimum and maximum

Table 3. Root Mean Square Difference (RMSD), Mean Bias (B), Correlation Coefficient (R) and Slope of the Linear Regression (S) Between Simulated and Observed SEE for the ISBA (ISB), H-TESSEL (HTE), CLM (CLM) Evaporation Modules as Well as the S92 and New (in Bold) Texture-Based r_{ss} Formulations, for Different Ranges of Clay Fraction: $f_{clay} < 0.10$ (1), $0.10 \leq f_{clay} < 0.20$ (2), $0.20 \leq f_{clay} < 0.30$ (3), $0.30 \leq f_{clay} < 0.40$ (4) and $f_{clay} \geq 0.40$ (5)

	RMSD					B					R					S				
f_{clay} range	ISB	HTE	CLM	S92	**New**	ISB	HTE	CLM	S92	**New**	ISB	HTE	CLM	S92	**New**	ISB	HTE	CLM	S92	**New**
1	0.41	0.49	0.39	0.32	**0.30**	0.29	0.09	0.20	0.16	**0.13**	0.41	0.51	0.53	0.57	**0.64**	0.21	0.89	0.64	0.49	**0.65**
2	0.42	0.48	0.42	0.31	**0.30**	0.34	0.18	0.18	0.19	**−0.06**	0.58	0.53	0.60	0.66	**0.62**	0.45	0.92	0.94	0.60	**0.73**
3	0.42	0.51	0.51	0.38	**0.38**	0.30	0.34	0.33	0.26	**0.16**	0.41	0.36	0.39	0.54	**0.50**	0.27	0.43	0.49	0.47	**0.59**
4	0.53	0.57	0.56	0.41	**0.32**	0.41	0.39	0.37	0.28	**−0.08**	0.23	0.28	0.33	0.34	**0.43**	0.19	0.39	0.48	0.27	**0.44**
5	0.42	0.48	0.48	0.38	**0.42**	0.28	0.32	0.30	0.20	**−0.09**	0.05	0.11	0.14	0.20	**0.36**	0.02	0.07	0.12	0.12	**0.46**
All	0.44	0.51	0.47	0.36	**0.34**	0.32	0.26	0.28	0.22	**0.01**	0.34	0.36	0.40	0.46	**0.51**	0.23	0.54	0.53	0.39	**0.58**

overall RMSD is estimated as 0.34 and 0.51 for the new r_{ss} and H-TESSEL, and the minimum and maximum overall B is estimated as 0.01 and 0.32 for the new r_{ss} and ISBA, respectively. Regarding the correlation with SEE measurements, the new r_{ss} outperforms the other four models with an overall R estimated as 0.51 compared to 0.34, 0.36, 0.40 and 0.46 for ISBA, H-TESSEL, CLM and S92 model, respectively. Note that S92 has a slightly larger R (0.54–0.66 versus 0.50–0.62) than the new r_{ss} for $0.1 \leq f_{clay} < 0.3$. This is probably due to a slight increase in the uncertainty in $\theta_{1/2}$ and $\Delta\theta_{1/2}^{-1}$ attributed to the PTFs of equations (28) and (29) applied to a limited range of soil texture ($0.1 \leq f_{clay} < 0.3$), over which the S92 r_{ss} formulation is deemed acceptable. The overall S between simulated and observed SEE is 0.23, 0.55, 0.53, 0.39 and 0.58, for ISBA, H-TESSEL, CLM, S92 and the new r_{ss}, respectively. S is systematically closer to 1 with the new r_{ss} than with S92 model. The relatively good overall perfomance of H-TESSEL and CLM is attributed to a S close to 1 for low clay content ($f_{clay} < 0.2$), while the S for both H-TESSEL and CLM decreases strongly for larger clay fractions down to $\sim$0.1 for $f_{clay} > 0.4$. For the entire texture range considered, the PTFs of equations (28) and (29) are more robust in terms of SEE estimates than the PTFs of the other four evaporation models.

The evaluation of ISBA, H-TESSEL, and CLM evaporation modules and S92 r_{ss} formulation highlights a significant bias in simulated SEE, especially for soils with a $f_{clay} > 0.2$. These four models were not derived from the data set used in the paper to derive the PTFs of equations (28) and (29), which most likely contributes to the better results of the new r_{ss} formulation. The point is that the parameters of the ISBA, H-TESSEL and CLM evaporation modules have pre-set values and, to date, there is no PTF for the *A* and *B* parameters in S92. Systematic biases in modeled SEE can also result from differing depth of the top soil layer used to compute evaporation compared to the observation depth. The depth of the top soil layer is 1 cm, 1.75 cm, 5 cm and 7 cm in ISBA [*Parrens et al*., 2014], CLM [*Tang and Riley*, 2013a], S92 [*Sellers et al*., 1992] and H-TESSEL [*Albergel et al*., 2012], respectively. Several studies have addressed the inconsistency of the sensing depth of soil moisture observations (about 0–5 cm in this study) with the top soil layer of land-surface models [e.g., *Parrens et al*., 2014]. For instance, the soil layer used to calibrate the S92 r_{ss} formulation is 0–5 cm in *Sellers et al*. [1992] and 0–1 cm in *Van de Griend and Owe* [1994], resulting in quite distinct values of *A* and *B*. In the same vein, *Merlin et al*. [2011] investigated the effect of the top soil layer thickness on the exponent *P* of the SEE formulation derived from *Lee and Pielke* [1992]. They found that *P* is an increasing (and quasi linear) function of the top soil layer thickness, so that for a given θ value, SEE is a decreasing function of the soil moisture sensing depth. The shallow depth (1 cm and 1.75 cm) of the top soil layer in ISBA and CLM may thus be (partly) responsible for the models overestimation. Given that in situ measurements are usually available in the 0–5 cm soil layer or deeper, the models that use a soil layer shallower than the 5 cm depth are difficult to evaluate, even though their validity over a wide range of soil types needs to be checked.

6. Summary and Perspectives

A meta-analysis data-driven approach is developed to represent SEE over a large range of soil and atmospheric conditions. SEE is modeled using a soil resistance (r_{ss}) formulation based on surface soil moisture (θ) and two resistance parameters $r_{ss,ref}$ and $\theta_{efolding}$. The data-driven approach aims to express both parameters as a function of observable data including meteorological forcing, cut-off soil moisture value $\theta_{1/2}$ at which SEE=0.5, and first derivative of SEE at $\theta_{1/2}$, named $\Delta\theta_{1/2}^{-1}$. An analytical relationship between ($r_{ss,ref}$; $\theta_{efolding}$) and ($\theta_{1/2}$; $\Delta\theta_{1/2}^{-1}$) is first built by running a soil energy balance model for two extreme conditions with $r_{ss} = 0$ and $r_{ss} \sim \infty$ from meteorological data solely, and by approaching the middle point from the two (wet and dry) reference points. Two different methods are then investigated to estimate the pair ($\theta_{1/2}$; $\Delta\theta_{1/2}^{-1}$) either from the time series of SEE and θ observations for a given site, or using the soil texture information for all sites.

The new model is tested across a bare soil database composed of more than 30 sites around the world, a clay fraction range of 0.02–0.56, a sand fraction range of 0.05–0.92, and about 30,000 acquisition times between 8 am and 6 pm local time. In an effort to test the regionalization capabilities of the model using readily available data, a parameterization of $\theta_{1/2}$ is proposed as a PTF of clay and sand percentages separately as well as using both in multi-regressional fashion, and $\Delta\theta_{1/2}^{-1}$ is set to a constant mean value for all sites with $n > 500$. The correlation coefficient between modeled and retrieved $\theta_{1/2}$ is 0.76 (absolute value) for both clay-based and sand-based PTFs, while the multilinear regression of $\theta_{1/2}$ with both clay and sand fractions (texture-based PTF) improves the correlation coefficient (0.81).

The new PTF-based r_{ss} model is compared in terms of SEE estimates with the PTFs of the evaporation modules of the ISBA, H-TESSEL, CLM surface schemes as well as the S92 r_{ss} formulation. All models are forced by the same input data set including meteorological data, texture information, and the near-surface (mostly 0–5 cm depth) soil moisture observations. The SEE simulated by ISBA, H-TESSEL, CLM and S92 models generally overestimates observations, especially for soils with a clay fraction larger than 0.2. In this texture range, the overestimation (about 0.30–0.40) is larger for ISBA, H-TESSEL and CLM, while the S92 r_{ss} formulation tends to reduce the mean bias (about 0.20–0.30) between modeled and observed SEE. The new texture-based r_{ss} formulation reduces the mean bias (0.0 in average) for all clay fraction classes. Moreover, the nonlinearities of the SEE(θ) relationship are relatively well represented by the new texture-based r_{ss} across the entire texture range. The shallow depth (1 cm and 1.75 cm) of the top soil layer in the ISBA and CLM models compared to the observation depth may be (partly) responsible for the models overestimation. Nonetheless, the ad hoc nature of the evaporation formulations in ISBA, H-TESSEL and CLM does not guarantee (in the absence of consistent validation) their validity over a wide range of soil types.

While the r_{ss} formulation developed in this paper is mostly semi-empirical, the strength of the approach relies on the capability to calibrate its parameters ($\theta_{1/2}$ and $\Delta\theta_{1/2}^{-1}$) from observable variables (SEE, θ, and meterological data). Specifically, four main benefits can be identified for future researches and applications:

1. the soil evaporation formulation as a function of r_{ss} has clear physical meaning, and thus, enables the implementation of the new evaporation model in a range of physically based land-surface models [*Pitman*, 2003]. Moreover, the SEE formulation of soil evaporation is fully consistent with the evaporation modules of operational models like the FAO-56 dual crop approach [*Allen*, 2000; *Lhomme et al*., 2015].
2. the proposed modeling framework is generic. It can be applied to characterize the variability of $\theta_{1/2}$ and $\Delta\theta_{1/2}^{-1}$ as a function of soil texture as it done in this paper. It can also be used to represent other variability factors such as the presence of stubble or mulch [*Sakaguchi and Zeng*, 2009], soil heterogeneity [*Or et al*., 2013], soil roughness, and shrinkage cracks in clayey soils. Further research is needed to account for the impact of the (seasonal, daily, instantaneous) variability of evaporative demand on $\theta_{1/2}$ and $\Delta\theta_{1/2}^{-1}$ through the time varying moisture profile in the top soil layer [*Merlin et al*., 2011].
3. such a meta-analysis data-driven approach is complementary to the upward modeling approaches based on fine physical knowledge and discretization of the soil layer. In particular, a key issue would be to interpret the variability of semi-empirical (but observed) $\theta_{1/2}$ and $\Delta\theta_{1/2}^{-1}$ in terms of the physical (but poorly observed in real field conditions) SHPs. Physically based soil water diffusion models [e.g., *Tang and Riley*, 2013b] will be very helpful in that direction.
4. given that a significant correlation exists between $\theta_{1/2}$ and sand and clay fractions, one could imagine a remote sensing approach for estimating surface soil texture from multi-sensor/multi-spectral remote sensing. In practice, several issues will need to be addressed beforehand such as the estimation of SEE from thermal infrared data [*Chanzy et al*., 1995; *Stefan et al*., 2015], the downscaling of microwave-derived θ [e.g., *Merlin et al*., 2013], and the partitioning between soil evaporation and plant transpiration from available remote sensing data [e.g., *Merlin et al*., 2014].

Appendix A: PTF-Derived SHPs

Soil moisture at field capacity is estimated as in *Noilhan and Mahfouf* [1996]:

$$\theta_{fc}=0.089\times(100f_{clay})^{0.3496} \tag{A1}$$

with f_{clay} being the clay fraction.

The residual soil moisture is estimated as in *Brisson and Perrier* [1991]:

$$\theta_{res}=0.15f_{clay} \tag{A2}$$

The soil moisture at saturation is estimated as in *Cosby et al*. [1984]:

$$\theta_{sat}=0.489-0.126f_{sand} \tag{A3}$$

with f_{sand} being the sand fraction.

Parameterized air entry pressure (in mm of water) at θ_{sat} is estimated as in *Cosby et al.* [1984]:

$$\psi_{sat} = -10 \times \exp\left(1.88 - 1.31 f_{sand}\right) \quad \text{(A4)}$$

The Clapp and Hornberger parameter is estimated as in *Cosby et al.* [1984]:

$$b_{CH} = 2.91 + 15.9 f_{clay} \quad \text{(A5)}$$

Appendix B: Soil Energy Balance Model

The evaporation model solves the classical energy budget equation over bare soil:

$$LE = Rn - G - H \quad \text{(B1)}$$

with LE (W m^{-2}) being the soil latent heat flux, H (W m^{-2}) the soil sensible heat flux, Rn (W m^{-2}) the soil net radiation and G (W m^{-2}) the ground conduction at 5 cm depth. Soil net radiation is expressed as:

$$Rn = (1 - a) R_g + \epsilon (R_a - \sigma T^4) \quad \text{(B2)}$$

with a being the soil albedo (set to 0.20), R_g (W m^{-2}) the incoming solar radiation, ϵ the soil emissivity (set to 0.97), R_a (W m^{-2}) the atmospheric longwave radiation, σ (Wm^{-2}K^{-4}) the Stephan-Boltzmann constant and T (K) the soil skin temperature. Downward atmospheric radiation at ground level is expressed as:

$$R_a = \epsilon_a \sigma T_a^4 \quad \text{(B3)}$$

with ϵ_a being the effective atmospheric emissivity, and T_a (K) the air temperature. The emissivity of clear skies is estimated as in *Brutsaert* [1975]:

$$\epsilon_a = 0.553 (e_a / 100)^{1/7} \quad \text{(B4)}$$

with:

$$e_a = e_{sat}(T_a)(h_a / 100) \quad \text{(B5)}$$

with h_a (%) being the air relative humidity and:

$$e_{sat}(T_a) = 611 \exp\left[17.27\,(T_a - 273.2)/(T_a - 35.9)\right] \quad \text{(B6)}$$

with T_a in K.

Ground conduction is estimated as a fraction of soil net radiation [*Choudhury et al.*, 1987; *Kustas and Daughtry*, 1990]:

$$G = C_G Rn \quad \text{(B7)}$$

with C_G a coefficient. Sensible heat flux is expressed as:

$$H = \rho C_P \frac{T - T_a}{r_{ah}} \quad \text{(B8)}$$

with the aerodynamic resistance being estimated as in *Choudhury et al.* [1986]:

$$r_{ah} = \frac{r_{ah0}}{(1 + Ri)^{\eta}} \quad \text{(B9)}$$

with r_{ah0} (s m^{-1}) being the neutral aerodynamic resistance, and Ri the Richardson number which represents the importance of free versus forced convection, and η a coefficient set to 0.75 in unstable conditions ($T > T_a$) and to 2 in stable conditions ($T < T_a$). The neutral r_{ah0} is computed as:

$$r_{ah0} = \frac{1}{k^2 u_a}\left[\ln\left(\frac{Z}{z_{0m}}\right)\right]^2 \quad \text{(B10)}$$

with k being the von Karman constant, u_a (m s^{-1}) the wind speed measured at the reference height Z (m) and z_{0m} (m) the momentum soil roughness. At all sites, z_{0m} is set to 0.001 m [*Yang et al.*, 2008; *Stefan et al.*, 2015]. The Richardson number is computed as:

$$Ri = \frac{5gZ(T-T_a)}{T_a u_a^2} \tag{B11}$$

with g (m s^{-2}) being the gravitational constant.

The energy balance equation (B1) is solved by initializing the surface soil temperature $T = T_a$, and by looking for the value of T which minimizes the cost function $F(T)$:

$$F(T) = (LE + H - Rn + G)^2 \tag{B12}$$

with LE being expressed as in equations (2)–(4) for the r_{ss}, α and β formulation, respectively.

Appendix C: Derivation of $\theta_{efolding}$

$\theta_{efolding}$ is derived by applying the constraint $\partial \mathrm{SEE}/\partial\theta(\theta_{1/2}) = \Delta\theta_{1/2}^{-1}$ (equation (17)). The first derivative of SEE is:

$$\frac{\partial \mathrm{SEE}}{\partial\theta} = \frac{r_{ah,wet}}{e_{sat}(T_{wet}) - e_a} \times \left[\frac{\dot{e}_{sat}(T)}{r_{ss}+r_{ah}} \times \frac{\partial T}{\partial\theta} + \frac{(e_{sat}(T)-e_a)r_{ss}}{(r_{ss}+r_{ah})^2} \times \frac{1}{\theta_{efolding}}\right] \tag{C1}$$

with $\dot{e}_{sat}(T)$ being the derivative of saturated vapor pressure with respect to T and $\partial T/\partial\theta$ the derivative of T with respect to θ. As $\partial T/\partial\theta$ is unknown, additional information is needed via the soil energy balance model expanded from equation (B1):

$$\frac{\rho C_P}{\gamma}\frac{e_{sat}(T)-e_a}{r_{ss}+r_{ah}} + \rho C_P \frac{T-T_a}{r_{ah}} = (1-C_G)[(1-a)R_g + \epsilon(R_a - \sigma T^4)] \tag{C2}$$

By applying the first derivative to equation (C2), it comes:

$$\frac{\rho C_P \dot{e}_{sat}(T)}{\gamma(r_{ss}+r_{ah})}\frac{\partial T}{\partial\theta} + \frac{\rho C_P(e_{sat}(T)-e_a)r_{ss}}{\gamma(r_{ss}+r_{ah})^2} \times \frac{1}{\theta_{efolding}} + \frac{\rho C_P}{r_{ah}}\frac{\partial T}{\partial\theta} = -4(1-C_G)\epsilon\sigma T^3 \frac{\partial T}{\partial\theta} \tag{C3}$$

and then:

$$\frac{\partial T}{\partial\theta} = \frac{f(\theta)}{\theta_{efolding}} \tag{C4}$$

with $f(\theta)$ being defined in equation (22). Finally, an expression of $\theta_{efolding}$ is obtained in equation (21) by inserting the above expression of $\partial T/\partial\theta$ in equation (C1).

Acknowledgments
This study was supported by the French Agence Nationale de la Recherche (MIXMOD-E project, ANR-13-JS06-0003-01) and the European Commission Horizon 2020 Programme for Research and Innovation (H2020) in the context of the Marie Skłodowska-Curie Research and Innovation Staff Exchange (RISE) action (REC projet, grant agreement no: 645642). We acknowledge the following sites of the European Flux Database (BELon, CHOe2, DEGeb, DEKli, DESeh, ESES2, FRAur, FRAvi, FRGri, FRLam, IECa1, ITBCi, ITCas, ITRo4), the following AmeriFlux sites (USArm, USDk1, USFwf, USIb1), the following OzFlux site (AUStu), the following long term observatories (AMMA, HOBE and SudMed), and the following short term intensive field campaigns (EFEDA, ReSeDa, Yaqui'08, HAPEX-Sahel, IHOP, Monsoon'90 and SGP'97) for their data records. This work utilized flux tower data collected by grants funded by the Australian Research Council (DP0772981, DP130101566, DP0344744 and LP100100073). Beringer is funded under an ARC Future Fellowship (FT110100602). Some support for OzFlux is provided through the Australia Terrestrial Ecosystem Research Network (TERN) (http://www.tern.org.au). The DMI (Danish Meteorological Institute) and Rasmus Jensen from HOBE are gratefully acknowledged. Funding for AmeriFlux data resources was provided by the U.S. Department of Energy Office of Science, Biological and Environmental Research and Atmospheric Radiation Measurement Program.

References

Alaoui, A., and B. Goetz (2008), Dye tracer and infiltration experiments to investigate macropore flow, *Geoderma*, *144*, 279–286, doi:10.1016/j.geoderma.2007.11.020.

Albergel, C., G. Balsamo, P. de Rosnay, J. Muñoz-Sabater, and S. Boussetta (2012), A bare ground evaporation revision in the ECMWF land-surface scheme: Evaluation of its impact using ground soil moisture and satellite microwave data, *Hydrol. Earth Syst. Sci.*, *16*, 3607–3620, doi:10.5194/hess-16-3607-2012.

Allen, R. G. (2000), Using the FAO-56 dual crop coefficient method over an irrigated region as part of an evapotranspiration intercomparison study, *J. Hydrol.*, *229*(1-2), 27–41, doi:10.1016/S0022-1694(99)00194-8.

Beringer, J., et al. (2011), SPECIAL––Savanna Patterns of Energy and Carbon Integrated Across the Landscape, *Bull. Am. Meteorol. Soc.*, *92*, 1467–1485.

Béziat, P., E. Ceschia, and G. Dedieu (2009), Carbon balance of a three crop succession over two cropland sites in South West France, *Agric. For. Meteorol.*, *149*(10), 1628–1645, doi:10.1016/j.agrformet.2009.05.004.

Bircher, S., N. Skou, K. H. Jensen, J. P. Walker, and L. Rasmussen (2012), A soil moisture and temperature network for SMOS validation in Western Denmark, *Hydrol. Earth Syst. Sci.*, *16*, 1445–1463, doi:10.5194/hess-16-1445-2012.

Bittelli, M., F. Ventura, G. S. Campbell, R. L. Snyder, F. Gallegati, and P. R. Pisa (2008), Coupling of heat, water vapor, and liquid water fluxes to compute evaporation in bare soils, *J. Hydrol.*, *362*, 191–205.

Braud, I., J. Noilhan, P. Mascart, P. Bessemoulin, R. Haverkamp, and M. Vauclin (1993), Bare ground surface heat and water exchanges under dry conditions: Observations and parameterization, *Boundary Layer Meteorol.*, *66*, 173–200.

Brisson, N., and A. Perrier (1991), A semiempirical model of bare soil evaporation for crop simulation models, *Water Resour. Res.*, *27*(5), 719–727.

Brutsaert, W. (1975), On a derivable formula for long-wave radiation from clear skies, *Water Resour. Res.*, *11*(5), 742–744.

Brutsaert, W. (2014), Daily evaporation from drying soil: Universal parameterization with similarity, *Water Resour. Res.*, *50*, 3206–3215, doi:10.1002/2013WR014872.

Cahill, A. T., M. B. Parlange, T. J. Jackson, P. O'Neill, and T. J. Schmugge (1999), Evaporation from nonvegetated surfaces: Surface aridity methods and passive microwave remote sensing, *J. Appl. Meteorol.*, *38*, 1346–1351.

Chanzy, A., and L. Bruckler (1993), Significance of soil surface moisture with respect to daily bare soil evaporation, *Water Resour. Res.*, *29*(4), 1113–1125.

Chanzy, A., L. Bruckler, and A. Perrier (1995), Soil evaporation monitoring: A possible synergism of microwave and infrared remote sensing, *J. Hydrol.*, *165*, 235–259.

Chanzy, A., M. Mumen, and G. Richard (2008), Accuracy of top soil moisture simulation using a mechanistic model with limited soil characterization, *Water Resour. Res.*, *44*, W03432, doi:10.1029/2006WR005765.

Chirouze, J., et al. (2014), Inter-comparison of four remote sensing based surface energy balance methods to retrieve surface evapotranspiration and water stress of irrigated fields in semi-arid climate, *Hydrol. Earth Syst. Sci.*, *18*, 1165–1188, doi:10.5194/hess-18-1165-2014.

Choudhury, B., R. J. Reginato, and S. B. Idso (1986), An analysis of infrared temperature observations over wheat and calculation of latent heat flux, *Agric. For. Meteorol.*, *37*, 75–88.

Choudhury, B., S. B. Idso, and R. J. Reginato (1987), Analysis of an empirical model for soil heat flux under a growing wheat crop for estimating evaporation by an infrared-temperature based energy balance equation, *Agric. For. Meteorol.*, *39*(4), 283–297.

Clapp, R. B., and G. M. Hornberger (1978), Empirical equations for some soil hydraulic properties, *Water Resour. Res*, *14*(4), 601–604.

Cosby, B., G. Hornberger, R. Clapp, and T. Ginn (1984), A statistical exploration of the relationships of soil moisture characteristics to the physical properties of soils, *Water Resour. Res*, *20*(6), 682–690.

Crow, W. T., W. P. Kustas, and J. H. Prueger (2008), Monitoring root-zone soil moisture through the assimilation of a thermal remote sensing-based soil moisture proxy into a water balance model, *Remote Sens. Environ.*, *112*, 1268–1281.

Dekic, L. J., D. T. Mihailovic, and B. Rajkovic (1995), A study of the sensitivity of bare soil evaporation schemes to soil surface wetness, using the coupled soil moisture and surface temperature prediction model, BARESOIL, *Meteorol. Atmos. Phys.*, *55*, 101–112.

Denef, K., I. D. Galdo, A. Venturi, and M. F. Cotrufo (2013), Assessment of soil C and N stocks and fractions across 11 European soils under varying land uses, *Open J. Soil Sci.*, *3*, 297–313.

Desborough, C. E., A. J. Pitman, and P. Irannejad (1996), Analysis of the relationship between bare soil evaporation and soil moisture simulated by 13 land surface schemes for a simple non-vegetated site, *Global Planet. Change*, *13*, 47–56.

Dickinson, R. E., A. Henderson-Sellers, P. J. Kennedy, and M. F. Wilson (1986), Biosphere-Atmosphere Transfer Scheme (BATS) for the NCAR Community Climate Model, Technical Note NCAR/TN-275-+STR, National Center for Atmospheric Research, Boulder, Colo., doi:10.5065/D6668B58.

Dore, S., M. Montes-Helu, S. Hart, B. Hungate, G. Koch, J. Moon, A. Finkral, and T. Kolb (2012), Recovery of southwestern ponderosa pine ecosystem carbon and water fluxes from thinning and stand replacing fire, *Global Change Biol.*, *18*(10), 3171–3185.

ECMWF (2014), *IFS Documentation, Part IV: Physical Processes*, vol. Cy40r1, Eur. Cent. for Medium-Range Weather Forecasts, Reading, U. K.

Er-Raki, S., A. Chehbouni, N. Guemouria, B. Duchemin, J. Ezzahar, and R. Hadria (2007), Combining FAO-56 model and ground-based remote sensing to estimate water consumptions of wheat crops in a semi-arid region, *Agric. Water Manage.*, *87*, 41–54.

Er-Raki, S., A. Chehbouni, G. Boulet, and D. Williams (2010), Using the dual approach of FAO-56 for partitioning ET into soil and plant components for olive orchards in a semi-arid region, *Agric. Water Manage.*, *97*(11), 1769–1778.

Feddes, R. A., et al. (2001), Modeling root water uptake in hydrological and climate models, *Bull. Am. Meteorol. Soc.*, *82*(12), 2797–2809.

Fischer, M. L., D. P. Billesbach, J. A. Berry, W. J. Riley, and M. S. Torn (2007), Spatiotemporal variations in growing season exchanges of co2, h2o, and sensible heat in agricultural fields of the southern great plains, *Earth Interact.*, *11*(17), 1–21.

Fritton, D. D., D. Kirkham, and R. H. Shaw (1967), Soil water and chloride redistribution under various evaporation potentials, *Soil Sci. Soc. Am. Proc.*, *31*, 599–603.

Garrigues, S., et al. (2015), Evaluation of land surface model simulations of evapotranspiration over a 12-year crop succession: Impact of soil hydraulic and vegetation properties, *Hydrol. Earth Syst. Sci.*, *19*(7), 3109–3131.

Gentine, P., D. Entekhabi, A. Chehbouni, G. Boulet, and B. Duchemin (2007), Analysis of evaporative fraction diurnal behaviour, *Agric. For. Meteorol.*, *143*, 13–29.

Good, S. P., D. Noone, and G. Bowen (2015), Hydrologic connectivity constrains partitioning of global terrestrial water fluxes, *Science*, *349*(6244), 175–177.

Heitman, J. L., X. Xiao, R. Horton, and T. J. Sauer (2008), Sensible heat measurements indicating depth and magnitude of subsurface soil water evaporation, *Water Resour. Res.*, *44*, W00D05, doi:10.1029/2008WR006961.

Jarlan, L., et al. (2015), Remote Sensing of Water Resources in the semi-arid Mediterranean areas: The Joint International Laboratory TREMA, *Int. J. Remote Sens.*, *36*(19–20), 4879–4917.

Kindler, R., et al. (2011), Dissolved carbon leaching from soil is a crucial component of the net ecosystem carbon balance, *Global Change Biol.*, *17*(2), 1167–1185, doi:10.1111/j.1365-2486.2010.02282.x.

Komatsu, T. S. (2003), Towards a robust phenomenological expression of evaporation efficiency for unsaturated soil surfaces, *J. Appl. Meteorol.*, *42*, 1330–1334.

Kool, D., N. Agam, N. Lazarovitch, J. L. Heitman, T. J. Sauer, and A. Ben-Gal (2014), A review of approaches for evapotranspiration partitioning, *Agric. For. Meteorol.*, *184*, 56–70.

Kustas, W. P., and C. S. T. Daughtry (1990), Estimation of the soil heat flux/net radiation ratio from spectral data, *Agric. For. Meteorol.*, *49*, 205–223.

Kustas, W. P., et al. (1991), An interdisciplinary field study of the energy and water fluxes in the atmosphere-biosphere system over semiarid rangelands: Description of some preliminary results, *Bull. Am. Meteorol. Soc.*, *72*, 1683–1705.

Kustas, W. P., X. Zhan, and T. J. Schmugge (1998), Combining optical and microwave remote sensing for mapping energy fluxes in a semiarid watershed, *Remote Sens. Environ.*, *64*, 116–131.

Kutsch, W. L., et al. (2010), The net biome production of full crop rotations in Europe, *Agric. Ecosyst. Environ.*, *139*, 336–345.

Lawrence, D. M., P. E. Thornton, K. W. Oleson, and G. B. Bonan (2007), The partitioning of evapotranspiration into transpiration, soil evaporation, and canopy evaporation in a GCM: Impacts on land-atmosphere interaction, *J. Hydrometeorol.*, *8*, 862–880.

Lee, T. J., and R. A. Pielke (1992), Estimating the soil surface specific humidity, *J. Appl. Meteorol.*, *31*, 480–484.

Lemone, M. A., F. Chen, J. G. Alfieri, R. H. Cuenca, Y. Hagimoto, P. Blanken, D. Niyogi, S. Kang, K. Davis, and R. L. Grossman (2007), NCAR/CU surface, soil, and vegetation observations during the international H2O Project 2002 field campaign, *Bull. Am. Meteorol. Soc.*, *88*, 65–81, doi:10.1175/BAMS-88-1-65.

Lhomme, J., N. Boudhina, M. Masmoudi, and A. Chehbouni (2015), Estimation of crop water requirements: Extending the one-step approach to dual crop coefficients, *Hydrol. Earth Syst. Sci.*, *19*, 3287–3299, doi:10.5194/hess-19-3287-2015.

Lintner, B., P. Gentine, K. Findell, and G. Salvucci (2015), The budyko and complementary relationships in an idealized model of large-scale land–atmosphere coupling, *Hydrol. Earth Syst. Sci.*, *19*(5), 2119–2131.

Mahfouf, J. F., and J. Noilhan (1991), Comparative study of various formulations of evaporation from bare soil using in situ data, *J. Appl. Meteorol.*, *30*, 1354–1365.

Mahrt, L., and H. Pan (1984), A two-layer model of soil hydrology, *Boundary Layer Meteorol.*, *29*, 1–20.

Manabe, S. (1969), Climate and the ocean circulation: I. The atmospheric circulation and the hydrology of the earth's surface, *Mon. Weather Rev.*, *97*(11), 739–774.

Marchesini, L. B., R. Casa, D. Papale, F. Pieruccetti, P. Stefani, N. Arriga, F. Mazzenga, and R. Valentini (2008), Evaluation of the greenhouse-gas reduction efficacy of a rapeseed (Brassica napa L.) biofuel crop and impact of agronomic techniques, in *EGU General Assembly 2008, Geophys. Res. Abstr.*, 10, EGU2008-A-11269.

Merlin, O. (2013), An original interpretation of the wet edge of the surface temperature-albedo space to estimate crop evapotranspiration (SEB-1S), and its validation over an irrigated area in northwestern Mexico, *Hydrol. Earth Syst. Sci.*, *17*, 3623–3637.

Merlin, O., and G. Chehbouni (2004), Different approaches in estimating heat flux using dual angle observations of radiative surface temperature, *Int. J. Remote Sens.*, *25*(1), 275–289.

Merlin, O., A. Al Bitar, V. Rivalland, P. Béziat, E. Ceschia, and G. Dedieu (2011), An analytical model of evaporation efficiency for unsaturated soil surfaces with an arbitrary thickness, *J. Appl. Meteorol. Climatol.*, *50*(2), 457–471, doi:10.1175/2010JAMC2418.1.

Merlin, O., M. J. Escorihuela, M. A. Mayoral, O. Hagolle, A. A. Bitar, and Y. Kerr (2013), Self-calibrated evaporation-based disaggregation of SMOS soil moisture: An evaluation study at 3 km and 100 m resolution in Catalunya, Spain, *Remote Sens. Environ.*, *130*, 25–38.

Merlin, O., J. Chirouze, A. Olioso, L. Jarlan, G. Chehbouni, and G. Boulet (2014), An image-based four-source surface energy balance model to estimate crop evapotranspiration from solar reflectance/thermal emission data (SEB-4S), *Agric. For. Meteorol.*, *184*, 188–203.

Mihailovic, D. T., B. Rajkovic, L. Dekic, R. A. Pielke, T. J. Lee, and Z. Ye (1995), The validation of various schemes for parameterizing evaporation from bare soil for use in meteorological models: A numerical study using in situ data, *Boundary Layer Meteorol.*, *76*, 259–289.

Milly, P. (1984), A simulation analysis of thermal effects on evaporation from soil, *Water Resour. Res.*, *20*(8), 1087–1098.

Moran, M. S., T. R. Clarke, Y. Inoue, and A. Vidal (1994), Estimating crop water deficit using the relation between surface-air temperature and spectral vegetation index, *Remote Sens. Environ.*, *49*, 246–263.

Nishida, K., R. R. Nemani, J. M. Glassy, and S. W. Running (2003), Development of an evapotranspiration index from Aqua/MODIS for monitoring surface moisture status, *IEEE Trans. Geosci. Remote Sens.*, *41*(2), 493–501.

Noilhan, J., and J.-F. Mahfouf (1996), The ISBA land surface parameterisation scheme, *Global Planet. Change*, *13*, 145–159.

Noilhan, J., and S. Planton (1989), A simple parameterization of land surface processes for meteorological models, *Mon. Weather Rev.*, *117*, 536–549.

Norman, J. M., W. P. Kustas, and K. S. Humes (1995), Source approach for estimating soil and vegetation energy fluxes in observations of directional radiometric surface temperature, *Agric. For. Meteorol.*, *77*, 263–293.

Novick, K., P. Stoy, G. Katul, D. Ellsworth, M. Siqueira, J. Juang, and R. Oren (2004), Carbon dioxide and water vapor exchange in a warm temperate grassland, *Oecologia*, *138*(2), 259–274.

Oleson, K. W., G.-Y. Niu, Z.-L. Yang, D. M. Lawrence, P. E. Thornton, P. J. Lawrence, R. Stockli, R. E. Dickinson, G. B. Bonan, and S. Levis (2007), *CLM3.5 Documentation*, Natl. Cent. for Atmos. Res., Boulder, Colo.

Oleson, K. W., et al. (2008), Improvements to the Community Land Model and their impact on the hydrological cycle, *J. Geophys. Res.*, *113*, G01021, doi:10.1029/2007JG000563.

Oleson, K. W., et al. (2013), Technical description of version 4.5 of the Community Land Model (CLM), *TN-503+STR*, Natl. Cent. for Atmos. Res., Boulder, Colo.

Olioso, A., et al. (2002), Monitoring energy and mass transfers during the Alpilles-ReSeDA experiment, *Agron. Sustainable Dev.*, *22*(6), 597–610, doi:10.1051/agro:2002051.

Or, D., P. Lehmann, E. Shahraeeni, and N. Shokri (2013), Advances in Soil Evaporation Physics - A Review, *Vadose Zone J.*, *12*(4), 1–16, doi:10.2136/vzj2012.0163.

Papale, D., et al. (2006), Towards a standardized processing of Net Ecosystem Exchange measured with eddy covariance technique: Algorithms and uncertainty estimation, *Biogeosciences*, *3*, 571–583.

Parrens, M., J.-F. Mahfouf, A. L. Barbu, and J.-C. Calvet (2014), Assimilation of surface soil moisture into a multilayer soil model: Design and evaluation at local scale, *Hydrol. Earth Syst. Sci.*, *18*, 673–689, doi:10.5194/hess-18-673-2014.

Passerat de Silans, A. (1986), Transferts de masse et de chaleur dans un sol stratifié soumis une excitation atmosphèrique naturelle. Comparaison modèle expérience, 205 pp., PhD thesis, Inst. Natl. Polytechnique de Grenoble, Grenoble, France.

Pellarin, T., J. Laurent, B. Cappelaere, B. Decharme, L. Descroix, and D. Ramier (2009), Hydrological modelling and associated microwave emission of a semi-arid region in South-western Niger, *J. Hydrol.*, *375*, 262–272.

Philip, J. R., and D. A. de Vries (1957), Moisture movement in porous materials under temperature gradients, *Eos Trans. AGU*, *38*, 222–232.

Pitman, A. J. (2003), The evolution of, and revolution in, land surface schemes designed for climate models, *Int. J. Climatol.*, *23*(5), 479–510.

Porporato, A., F. Laio, L. Ridolfi, and I. Rodriguez-Iturbe (2001), Plants in water-controlled ecosystems: Active role in hydrologic processes and response to water stress: III. Vegetation water stress, *Adv. Water Resour.*, *24*(7), 725–744.

Prévot, L., R. Bernard, O. Taconet, and D. V. Madjar (1984), Evaporation from a bare soil evaluated using a bare soil water transfer model and remotely sensed surface soil moisture data, *Water Resour. Res.*, *20*(2), 311–316.

Robock, A., K. Y. Vinnikov, C. A. Schlosser, N. A. Speranskaya, and Y. Xue (1995), Use of midlatitude soil moisture and meteorological observations to validate soil moisture simulations with Biosphere and Bucket models, *J. Clim.*, *8*, 15–35.

Roerink, G. J., Z. Su, and M. Menenti (2000), S-SEBI: A simple remote sensing algorithm to estimate the surface energy balance, *Phys. Chem. Earth, Part B*, *25*(2), 147–157.

Sakaguchi, K., and X. Zeng (2009), Effects of soil wetness, plant litter, and under-canopy atmospheric stability on ground evaporation in the Community Land Model (CLM3.5), *J. Geophys. Res.*, *114*, D01107, doi:10.1029/2008JD010834.

Santanello, J. A., C. D. Peters-Lidard, M. E. Garcia, D. M. Mocko, M. A. Tischler, M. S. Moran, and D. Thoma (2007), Using remotely-sensed estimates of soil moisture to infer soil texture and hydraulic properties across a semi-arid watershed, *Remote Sens. Environ.*, *110*, 79–97.

Schlesinger, W. H., and S. Jasechko (2014), Transpiration in the global water cycle, *Agric. For. Meteorol.*, *189*, 115–117.

Sellers, P. J., M. D. Heiser, and F. G. Hall (1992), Relations between surface conductance and spectral vegetation indices at intermediate ($100\ m^2$ to $15\ km^2$) length scales, *J. Geophys. Res.*, *97*(D17), 19,033–19,059.

Sellers, P. J., D. A. Randall, G. J. Collatz, J. A. Berry, C. B. Field, D. A. Dazlich, C. Zhang, G. D. Collelo, and L. Bounoua (1996), A revised land surface parameterization (SiB2) for atmospheric GCMs. Part I: Model formulation, *J. Clim.*, *9*, 676–705.

Shahraeeni, E., P. Lehmann, and D. Or (2012), Coupling of evaporative fluxes from drying porous surfaces with air boundary layer: Characteristics of evaporation from discrete pores, *Water Resour. Res.*, *48*, W09525, doi:10.1029/2012WR011857.

Shuttleworth, W. J., and J. S. Wallace (1985), Evaporation from sparse canopies-an energy combination theory, *Q. J. R. Meteorol. Soc.*, *111*, 839–855.

Simmonds, L. P., and E. J. Burke (1999), Application of a coupled microwave, energy and water transfer model to relate passive microwave emission from bare soils to near-surface water content and evaporation, *Hydrol. Earth Syst. Sci.*, *3*(1), 31–38.

Sivapalan, M., G. Bloschl, L. Zhang, and R. Vertessy (2003), Downward approach to hydrological prediction, *Hydrol. Processes*, *17*, 2101–2111.

Smits, K. M., V. V. Ngo, A. Cihan, T. Sakaki, and T. H. Illangasekare (2012), An evaluation of models of bare soil evaporation formulated with different land surface boundary conditions and assumptions, *Water Resour. Res.*, *48*, W12526, doi:10.1029/2012WR012113.

Soarès, J., R. Bernard, O. Taconet, D. Vidal-Madjar, and A. Weill. (1988), Estimation of bare soil evaporation from airborne measurements, *J. Hydrol.*, *99*, 281–296.

Stefan, V. G., O. Merlin, S. Er-Raki, M.-J. Escorihuela, and S. Khabba (2015), Consistency between in situ, model-derived and high-resolution-image-based soil temperature endmembers: Towards a robust data-based model for multi-resolution monitoring of crop evapotranspiration, *Remote Sens.*, *7*(8), 10,444–10,479.

Stöckli, R., D. M. Lawrence, G.-Y. Niu, K. W. Oleson, P. E. Thornton, Z.-L. Yang, G. B. Bonan, A. S. Denning, and S. W. Running (2008), Use of FLUXNET in the Community Land Model development, *J. Geophys. Res.*, *113*, G01025, doi:10.1029/2007JG000562.

Su, Z. (2002), The Surface Energy Balance System (SEBS) for estimation of turbulent heat fluxes, *Hydrol. Earth Syst. Sci.*, *6*(1), 85–99.

Sun, S. F. (1982), Moisture and heat transport in a soil layer forced by atmospheric conditions, MS thesis, 72 pp., Univ. of Conn., Storrs.

Tang, J., and W. J. Riley (2013a), Impacts of a new bare-soil evaporation formulation on site, regional, and global surface energy and water budgets in CLM4, *J. Adv. Model. Earth Syst.*, *5*, 558–571, doi:10.1002/jame.20034.

Tang, J., and W. J. Riley (2013b), A new top boundary condition for modeling surface diffusive exchange of a generic volatile tracer: Theoretical analysis and application to soil evaporation, *Hydrol. Earth Syst. Sci.*, *17*, 873–893, doi:10.5194/hess-17-873-2013.

Timmermans, W. J., W. P. Kustas, M. C. Anderson, and A. N. French (2007), An intercomparison of the Surface Energy Balance Algorithm for Land (SEBAL) and the Two-Source Energy Balance (TSEB) modeling schemes, *Remote Sens. Environ.*, *108*, 369–384.

Twine, T. E., W. Kustas, J. Norman, D. Cook, P. Houser, T. Meyers, J. Prueger, P. Starks, and M. Wesely (2000), Correcting eddy-covariance flux underestimates over a grassland, *Agric. For. Meteorol.*, *103*(3), 279–300.

Van de Griend, A. A., and M. Owe (1994), Bare soil surface resistance to evaporation by vapor diffusion under semiarid conditions, *Water Resour. Res.*, *30*(2), 181–188.

Van den Hoof, C., E. Hanert, and P. L. Vidale (2011), Simulating dynamic crop growth with an adapted land surface model––JULES-SUCROS: Model development and validation, *Agric. For. Meteorol.*, *151*, 137–153.

Van den Hurk, B. J. J. M., P. Viterbo, A. C. M. Beljaars, and A. K. Betts (2000), Offline validation of the ERA40 surface scheme, *European Centre for Medium-Range Weather Forecasts, Tech. Memo. 295*, Reading, U. K.

Vidale, L., and R. Stöckli (2005), Prognostic canopy air space solutions for land surface exchanges, *Theor. Appl. Climatol.*, *80*(2-4), 245–257.

Viterbo, P., and A. C. M. Beljaars (1995), An improved land surface parametrization scheme in the ECMWF model and its validation, *European Centre for Medium-Range Weather Forecasts, Tech. Rep. 75*, Res. Dep., ECMWF, Reading, U. K.

Wallace, J. S., S. J. Allen, J. H. C. Gash, C. J. Holwill, and C. R. Lloyd (1993), Components of the energy and water balance at the HAPEX-Sahel southern super-site, in *Proceedings of the Yokohama Symposium*, vol. 212, International Association of Hydrological Sciences Publ., pp. 365–371, Yokohama, Japan.

Walmsley, D. C., J. Siemens, R. Kindler, L. Kirwan, K. Kaiser, M. Saunders, M. Kaupenjohann, and B. A. Osborne (2011), Dissolved carbon leaching from an Irish cropland soil is increased by reduced tillage and cover cropping, *Agric. Ecosyst. Environ.*, *142*, 393–402.

Wang, L., S. P. Good, and K. K. Caylor (2014), Global synthesis of vegetation control on evapotranspiration partitioning, *Geophys. Res. Lett.*, *41*, 6753–6757, doi:10.1002/2014GL061439.

Wetzel, P. J., and J.-T. Chang (1988), Evapotranspiration from nonuniform surfaces: A first approach for short-term numerical weather prediction, *Mon. Weather Rev.*, *116*, 600–621.

Williams, D. G., et al. (2004), Evapotranspiration components determined by stable isotope, sap flow and eddy covariance technique, *Agric. For. Meteorol.*, *125*, 241–258.

Wood, E. F., D. P. Lettenmaier, and V. G. Zartarian (1992), A land-surface hydrology parameterization with subgrid variability for general circulation models, *J. Geophys. Res.*, *97*(D3), 2717–2728.

Wu, C., et al. (2012), An underestimated role of precipitation frequency in regulating summer soil moisture, *Environ. Res. Lett.*, *7*(2), 024011.

Yamanaka, T., A. Takeda, and J. Shimada (1998), Evaporation beneath the soil surface: Some observational evidence and numerical experiments, *Hydrol. Processes*, *12*, 2193–2203.

Yang, K., T. Koike, H. Ishikawa, J. Kim, X. Li, H. Liu, S. Liu, Y. Ma, and J. Wang (2008), Turbulent flux transfer over bare-soil surfaces: Characteristics and parameterization, *J. Appl. Meteorol. Climatol.*, *47*(1), 276–290.

Yang, Z.-L., R. E. Dickinson, W. J. Shuttleworth, and M. Shaikh (1998), Treatment of soil, vegetation and snow in land surface models: A test of the biosphere-atmosphere transfer scheme with the hapex-mobilhy, abracos and russian data, *J. Hydrol.*, *212-213*, 109–127.

Ye, Z., and R. A. Pielke (1993), Atmospheric parameterization of evaporation from non-plant-covered surfaces, *J. Appl. Meteorol.*, *32*, 1248–1258.

Zribi, M., A. Chahbi, M. Shabou, Z. Lili-Chabaane, B. Duchemin, N. Baghdadi, R. Amri, and A. Chehbouni (2011), Soil surface moisture estimation over a semi-arid region using ENVISAT ASAR radar data for soil evaporation evaluation, *Hydrol. Earth Syst. Sci.*, *15*, 345–358.